



Evaluation of methods used for simulation of heat-affected zones in duplex stainless steels

E. M. Westin¹ · L. G. Westerberg²

Received: 26 September 2023 / Accepted: 25 January 2024
© The Author(s) 2024

Abstract

The weldability of duplex stainless steels partly depends on the ferritization of the high-temperature heat-affected zone (HT-HAZ). This area is rather narrow, and it can be challenging to visualize and determine its actual impact on the properties. To address this, various methods were applied to study the grain growth and austenite reformation in the HT-HAZ of the lean duplex grade UNS S32101. Thermo-mechanical Gleeble[®] simulations were conducted at 1360 °C with different holding times and cooling rates. Subsequently, the grain size and ferrite content were measured on polished and etched cross-sections. Bead-on-plate welds were performed on the same heat of 6-mm plate thickness using the gas tungsten arc welding (GTAW) process. The shielding gas was Ar + 0–8% N₂ to illustrate the effect of nitrogen additions on the HT-HAZ morphology. The arc was either stationary, welding at one spot for 0.5–120 s, or travelling at different speeds to generate varying heat inputs and temperature gradients. The thermo-mechanical simulations approximated the results obtained by travelling arc welding and allowed for a more comprehensive investigation. Stationary arc welding was not suitable for HT-HAZ studies as it quickly caused nitrogen depletion and resulted in significantly higher ferrite contents compared to the travelling arc welds.

Keywords Duplex stainless steel · Welding · GTAW · HAZ · Nitrogen · Phase balance · Physical simulation

1 Introduction

1.1 Duplex stainless steels and their weldability

Duplex stainless steels offer an economical combination of strength and corrosion resistance, achieved through equal proportions of ferrite and austenite. The ferrite matrix provides strength and resistance to stress corrosion cracking, while the austenite contributes good ductility and pitting resistance. The toughness and corrosion performance are consequently dependent on the phase balance [1]. The fractions of austenite and ferrite are nearly equal in the as-delivered condition due to an engineered composition and optimized heat treatment. The amounts in the weld metal

and heat-affected zone (HAZ) are, on the other hand, determined by the chemical composition and the thermal history.

To guarantee that the properties are retained also after welding, the weld metal ferrite content is commonly specified at 30–70 vol.-% [2] or stricter with 35–65 vol.-% [3–6]. It is generally recommended to use a filler metal that is over-alloyed in nickel to ensure sufficient austenite formation [7]. If there are requirements on the phase balance, autogenous welding of duplex stainless steels may not be possible. Especially the alloys UNS S32304, UNS S31803, and UNS S32205 have been reported to result in high ferrite contents in the weld metal and HAZ [8–10].

Duplex stainless steels solidify in the ferritic mode and austenite forms through diffusion-controlled transformation in the solid phase during cooling [11]. Precipitation first occurs at the grain boundaries, followed by Widmanstätten plates, and finally as intragranular precipitates [12–15]. The austenite formation has been found to be controlled by redistribution of nitrogen rather than diffusion of the slower diffusing metallic elements [16, 17]. The weldability of most available commercial grades has been improved appreciably as compared to the earlier generations of duplex steels by increasing the nitrogen content [18–20].

✉ L. G. Westerberg
goran.westerberg@ltu.se

E. M. Westin
elin.westin@voestalpine.com

¹ voestalpine Böhler Welding Austria GmbH,
Böhler-Welding-Str. 1, 8605 Kapfenberg, Austria

² Division of Fluid and Experimental Mechanics, Luleå
University of Technology, 97187 Luleå, Sweden

In previous duplex alloy versions, the HAZ suffered from ferritization and excessive grain growth. The low austenite reformation had a negative impact on the corrosion resistance and mechanical properties. The higher nitrogen content in modern duplex stainless steels influences the driving force for austenite formation and promotes the formation of austenite at higher temperatures [21, 22]. Additionally, nitrogen alloying reduces the fully ferritic range between the ferrite solidus and ferrite solvus. Since austenite primarily forms on ferrite grain boundaries, the enhanced resistance to ferrite grain growth in the HAZ increases the number of nucleation sites [23]. In autogenous welding, where no filler metal is added, nitrogen plays a crucial role for the final phase balance in both the weld metal and HAZ.

While both the essential alloying elements nitrogen and nickel act as strong austenite formers, interstitial nitrogen can reach longer diffusion distances and has a greater effect on austenite reformation than nickel [24]. During a weld thermal cycle, the diffusion distance of nitrogen with a diffusion rate of 1.3×10^{-6} cm²/s is around 50–100 µm, whereas nickel, with a rate of 3.9×10^{-11} cm²/s, only reaches approximately 4.4 µm [25]. High nitrogen contents may thus reduce the influence of the cooling rates on microstructure, making the material less sensitive to welding with low heat input [26].

1.2 Effect of nitrogen

While nitrogen contributes strength to materials as an interstitial element, duplex stainless steels are primarily alloyed with nitrogen for its positive effect on the phase balance. Ogawa and Koseki [19] stated that an increase in the nitrogen content of duplex stainless steels enhances the pitting corrosion resistance of the weld metal and HAZ. Kokawa et al. [27] reported a linear increase of austenite formation with the weld metal nitrogen content. Consequently, nitrogen loss during welding and solidification of the weld metal can have a negative influence on the final phase balance and corrosion performance [28].

In gas tungsten arc welding (GTAW), nitrogen loss particularly occurs when using pure argon (Ar) as shielding and backing gas, while nitrogen additions to the shielding gas and nitrogen-based backing gas (N₂ + 0–10% H₂) lead to improved austenite formation and pitting resistance [21, 29–34]. The nitrogen in the shielding gas dissociates at the arc plasma temperature and the atomic nitrogen can dissolve in the molten pool [35]. The nitrogen content is practically limited to 2–3% due to increased wear of the tungsten electrode. Nitrogen has in addition been reported to have a positive influence as both shielding and backing gas when laser welding autogenously [33, 36–39] and in wire-assisted additive manufacturing [34, 40].

The HAZ is mainly affected by the base metal composition and heat input. For a given chemical composition, the

austenite reformation depends primarily on the cooling rate and grain size [41]. The pitting resistance of the HAZ may be improved by increased nitrogen content in the parent material, higher heat input, and slower cooling rates [23, 42–45]. It is not as clear if substantial nitrogen loss occurs from the HAZ in normal welding with or without nitrogen additions to the shielding gas. However, Hosseini and Karlsson [46] demonstrated that nitrogen loss in a super duplex material occurred at a distance of up to 150 µm already after 30 s of arc heat treatment with Ar. Varbai et al. [47] performed Gleeble[®] HT-HAZ simulations on UNS S32205 with nitrogen as ambient atmosphere and concluded that a fully austenitic surface layer of approximately 70-µm thickness formed after 60 s due to nitrogen absorption. This would indicate the nitrogen diffusion at an excess of nitrogen. Electron microprobe analysis (EPMA) measurements have revealed a gradual depletion of nitrogen in the HT-HAZ over time during stationary welding of UNS S32101 [48]. In contrast, no significant depletion was observed in travelling arc welding [49].

1.3 Chromium nitrides

At the temperatures where duplex alloys are fully ferritic, nitrogen exhibits high diffusivity and solubility. Subsequent cooling leads to a decrease in the diffusion rate and solubility of nitrogen in the ferrite phase, causing precipitation of chromium-rich nitrides within the ferrite grains [50]. Nitrides are unavoidable in the HAZ and can to various extents also be found in the weld metal [51]. The most reported and thermally stable type is Cr₂N [23, 50, 52–60]. These nitrides precipitate between 700 and 900 °C due to a sharp decrease in the nitrogen solubility of the ferrite phase during the cooling process.

Although it is not possible to completely eliminate the formation of Cr₂N, slower cooling rates reduce their quantity by promoting austenite formation that dissolves nitrogen [61, 62]. The precipitation leads to chromium-depleted regions in the ferrite and ferrite-ferrite grain boundaries, which are preferentially attacked in highly corrosive environments and corrosion testing of weld cross-sections [42, 50, 53–55, 63–65]. The austenite formed at grain boundaries hinders the corrosion attack, and the propagation primarily occurs in the nitride-rich centers of the grains [17].

In addition to hexagonal Cr₂N, cubic CrN in the form of film or platelets has also been found in duplex welds and HAZs [52, 53, 55, 66, 67]. Pettersson et al. [66] suggested that CrN forms through crystallographically favored nucleation, before the precipitation of either austenite or Cr₂N, when the cooling is very rapid and the ferrite is heavily supersaturated. This condition could be reached in HT-HAZ simulations where the cooling rate can be rapid through water quenching.

Yang et al. [67] found more CrN than Cr₂N at higher cooling rates in simulated HT-HAZ in UNS S32205. Hertzman et al. [52] showed with thermodynamic calculations that CrN is less stable than Cr₂N. More recent work by Hölländer Pettersson et al. [68] confirmed intragranular presence of CrN with a cubic halite-type structure and clusters of CrN-Cr₂N where rod-shaped trigonal Cr₂N particles had nucleated on plates of CrN. In a subsequent heat treatment at 900 °C, the metastable CrN served as nucleation sites for more thermodynamically stable Cr₂N and intragranular idiomorphic secondary austenite. CrN has, in contrast to Cr₂N, been reported to only have a limited effect on the pitting corrosion resistance [53]. This is possibly due to less chromium depletion in the surrounding matrix.

1.4 HAZ morphology

Due to different temperatures obtained in the material, the HAZ consists of different structures ranging from the fusion line out to the unaffected parent metal [69]. The structural changes in the HAZ of duplex weldments can degrade the toughness and corrosion resistance to varying extents. The potential problems include excessive grain growth, improper phase balance, and precipitation of chromium carbides, nitrides, and intermetallic compounds [70].

It may be appropriate to distinguish the high-temperature HAZ (HT-HAZ) from the low-temperature HAZ (LT-HAZ). According to Brandi [71], the temperature range for LT-HAZ is 950 to 650 °C, while the HT-HAZ extends from solidus temperature to approximately 1000 °C. The HT-HAZ will reach a temperature where much or all of the austenite has transformed into ferrite and, when not pinned by austenite, enabling ferrite grain growth [72]. This makes this area clearly visible, while the LT-HAZ is less prominent with only minor change. Although the ferritization primarily occurs at temperatures higher than 1250 °C, the cooling time from 1200 to 800 °C, $t_{12/8}$, is sometimes used to correlate the ferrite/austenite balance in the HT-HAZ [3].

The width of the HT-HAZ is in the order of 1–2 grain diameters and depends on both composition (and associated thermal width of the ferrite phase field) and the time available for dissolution of the austenite [73]. Although the width can normally easily be measured, it varies with the welding conditions and the chemical composition of the base material [74]. With high nitrogen contents and rapid austenite formation, it can be challenging to identify the exact location of the fusion line and thus not be possible to determine the precise width [49]. If the cooling rate, from a fully ferritic or partly ferritic region, is too rapid to allow for the nitrogen diffusion-driven phase transformation, the time is insufficient for desirable austenite formation, and the resulting HT-HAZ becomes predominantly ferritic [52]. The material composition, thickness, and heat input affect the ferrite grain

size, austenite growth mechanism, nucleation rate, nucleation sites, and composition of precipitated phases [52].

The LT-HAZ does not show ferritization and associated grain growth but reaches temperatures where sigma and chi phases may form due to slow cooling or repeated reheating to 800–1000 °C [71, 75–78]. However, in most welding procedures, the time spent in this susceptible temperature range is insufficient to measure any additional deterioration in mechanical properties or corrosion resistance compared to the HT-HAZ.

1.5 HT-HAZ simulation

As the HT-HAZ is narrow, thermo-mechanical simulation can be used to create a sufficiently large area of uniform structure for many types of testing. Physical simulations of the HAZ have successfully been carried out using Gleeble® simulators and similar equipment [16, 23, 24, 28, 46, 47, 55, 67, 79–86]. The alloys UNS S32101, UNS S32304, UNS S31805, UNS S32205, and UNS S32750 have all been reported to maintain a ferritic single-phase region below the solidus [16, 72, 81, 87]. The studies mainly concern ferritization and grain growth in the fully ferritic range, investigating the effect of cooling rate on austenite reformation and impact toughness. Such investigations confirm the positive role of nitrogen in promoting austenite reformation in the HT-HAZ by increasing the austenite transformation temperature and inhibiting grain growth.

The main challenge with thermo-mechanical simulation is to heat the samples to the correct ferritization temperature where all austenite is dissolved. Otherwise, a banded structure consisting of partially transformed austenite may still be found [24, 41, 67]. This could result in pinned ferrite grain boundaries, inhibiting further growth and leading to higher impact toughness values than in the actual HT-HAZ [86]. Conversely, if the temperature becomes too high (e.g., overshooting), the sample may collapse (melt).

The arc heat treatment method developed by Hosseini et al. [69] is a more advanced type of stationary arc welding. They have used it to create TTT diagrams and study particles formed in duplex stainless steels [46], super duplex stainless steels [88, 89], duplex flux-cored arc welds [90], and additive manufacturing with super duplex wires [91]. The main advantage is the simultaneous heat treatment at all temperatures from room temperature to liquidus temperature achieving a graded microstructure within a single sample [69]. It is also possible to determine which region is most susceptible to pitting corrosion. The primary limitation of the arc heat treatment technique is that longer arc times are required (> 10 min), which means that the weld metal and HT-HAZ are depleted by nitrogen. The inventors noted that it unfortunately not possible to compensate for nitrogen loss by adding nitrogen to the

shielding gas, as the weld puddle becomes oversaturated and unstable at long welding times.

1.6 Aim

Thermo-mechanical simulation, commonly employed for studying HAZ properties, relies on the availability of special equipment. Therefore, other methods may be considered as alternatives. Stationary GTAW welding on the same spot for different durations has previously been applied to investigate the weld metal shape, nitrogen content, and ferrite fractions in duplex stainless steels [92–95]. Hosseini et al. [69] used the arc heat treatment method to investigate the resulting microstructure in the HAZ of different duplex alloys [46, 88–91]. The aim of this work was to evaluate the relevance of stationary arc welding bead-on-plate for 0–120 s and Gleeble® simulated HT-HAZ compared to regular travelling arc welding bead-on-plate. Four different shielding gases were applied (Ar, Ar+2% N₂, Ar+5% N₂, Ar+8% N₂) to study if the weld metal nitrogen content has an effect on the austenite reformation in the HT-HAZ. The methods for simulating HAZs are applicable for all modern duplex alloys. In this work, the lean duplex stainless steel UNS S32101 was selected because this grade exhibits good weldability and is commonly found in various applications where the welding is performed without fillers [33]. The higher nitrogen content increases the austenite reformation ability in the HT-HAZ compared to UNS S32304 and UNS S32205. The alloy UNS S32750 contains more nitrogen but requires addition of over-alloyed filler metal to compensate for segregation of molybdenum in the weld metal.

2 Experimental

2.1 Base material

The chemical composition of the 6-mm-thick base material plate used in this work is shown in Table 1.

2.2 Welding

Welding was performed autogenously (without filler) bead-on-plate with the GTAW process. The equipment was a modified EWM TIG 450 DC-P (EWM AG, Mündersbach, Germany) and the parameters logged using a WeldAnalyst® Version 4 (HKL Prozesstechnik, Halle, Germany). The electrode was of W-Th type with 60° sharpening angle, and it was reground between each new gas combination or more often as needed. The electrode stick-out was 5 mm and the arc length 2.5 mm.

Stationary (non-moving) arc welding was performed with four different shielding gases: Ar, Ar+2% N₂, Ar+5% N₂, and Ar+8% N₂. The gas flow rate was 15 l/min. A pre-gas flow was applied for 5 s before the arc was ignited and a post-flow for 8 s followed after extinction. Ninety percent N₂+10% H₂ was used as backing gas with a flow rate of 20 l/min. For the 6-mm-thick plate, however, the effect of the backing gas on the weld bead itself would be considered to be negligible. The welding current was permanently set to 80 A. The voltage depended on the type of shielding gas that was used, and the average decreased with increased welding time due to high initial values (Table 2). The welding proceeded with different welding times; 0.5, 1, 2.5, 5, 10, 20, 60, and 120 s. These were adjusted with a digital circuit-breaking relay. At least ten welds were produced with each combination of shielding gas and welding time. To compare the appearance of the HAZ of the stationary arc with real travelling arc welds, autogenous GTAW was carried out bead-on-plate using the same shielding gas types (Table 3). As higher nitrogen additions are impractical due to the excessive wear of the tungsten electrode, the number of samples were reduced for Ar+5% N₂ and Ar+8% N₂.

2.3 Measurement of nitrogen content

To determine the weld metal nitrogen content, drilled chips were analyzed using the Leco melt evaporation method. It was possible to measure the nitrogen content in all stationary welds welded for 5 s or longer and for all the travelling arc welds. Control of the drilled depth was performed to ensure that only weld metal was included.

The shortest stationary welding times (0.5, 1.0, and 2.5 s) resulted in welds that were somewhat too small to machine for Leco analysis. The weld metal nitrogen of stationary

Table 2 Average voltage for stationary arc welding

Time s	Average voltage, V			
	Ar	Ar+2% N ₂	Ar+5% N ₂	Ar+8% N ₂
0.5	12.4	12.6	12.8	13.2
1	12.2	12.6	12.6	12.8
2.5	11.8	12.1	12.2	12.5
5	11.4	11.7	11.9	12.3
10	10.9	10.9	11.6	11.9
20	10.7	10.8	11.5	11.5
60	10.6	10.8	11.1	11.5
120	10.6	10.8	11.1	11.6

Table 1 Chemical composition of the base material, wt.-%

Material	C	Si	Mn	P	S	Cr	Ni	Mo	Cu	N
UNS S32101	0.025	0.70	5.34	0.016	0.001	21.35	1.52	0.30	0.31	0.226

Table 3 Welding parameters for travelling arc welding

Shielding gas	Voltage, V	Current, A	Welding speed, mm/s	Arc energy, kJ/mm
Ar	10.7	98.4	2.75	0.38
Ar	10.3	79.0	1.71	0.48
Ar	10.7	98.0	1.84	0.57
Ar	10.6	98.6	1.56	0.67
Ar	10.7	97.9	1.20	0.87
Ar	10.2	79.3	0.85	0.96
Ar	10.7	98.0	0.88	1.19
Ar+2% N ₂	11.7	99.9	2.69	0.43
Ar+2% N ₂	11.2	79.5	1.70	0.52
Ar+2% N ₂	11.5	100.1	1.83	0.63
Ar+2% N ₂	11.4	100.1	1.30	0.88
Ar+2% N ₂	10.3	79.3	0.92	0.90
Ar+2% N ₂	11.3	99.9	1.13	1.00
Ar+2% N ₂	11.4	99.9	0.95	1.20
Ar+5% N ₂	10.8	79.1	1.72	0.50
Ar+5% N ₂	11.3	80.0	0.94	0.96
Ar+8% N ₂	12.0	80.3	1.70	0.55
Ar+8% N ₂	11.1	79.1	0.95	0.93

arc welds was, for this reason, additionally measured using electron probe microanalysis (EPMA) (ARL-SEMQ, DELL GX1-500, Corr-Control, Avesta, Sweden) [48, 96]. As comparison, samples of travelling arc welds were also examined. The modified instrument contained six wavelength dispersive spectrometers modified for mapping, each containing two crystals. Lead stearate (PbSD) was used as crystal material. The calibration for nitrogen was performed with an experimental set of nine martensitic Fe–C–N alloys with nitrogen contents varying from 0.037 to 0.435% [97]. In

addition, BN (43% B + 57% N) was used to adjust the wavelength of the PbSD crystal. EPMA mapping was performed on cross-sections polished to 3 μm in the last step. The sample current was 8000 nA and the voltage 10 kV. Mapping of nitrogen was carried out by an electron beam of 1- μm diameter scanned over 20 \times 20 or 50 \times 50 μm to determine the average content.

2.4 Gleeble® simulation

To create a sufficiently large area of uniform microstructure, thermo-mechanical HT-HAZ simulations were performed using a resistance-heated Gleeble® 3500 (Dynamic Systems Inc., Troy, New York). Waterjet cut specimens of 6 \times 12 \times 120 mm size were individually heated to 1360 °C to assure full ferritization and held for 0, 5, 10, or 30 s (Fig. 1a). The goal was to obtain a range of equiaxed ferrite grain sizes. The temperature was measured with thermocouples of K-type ultrasonically welded to the sample. The peak temperature of 1360 °C was experimentally set to the highest feasible point without inducing partial melting of the sample. Pettersson et al. [72] demonstrated that UNS S32101 is fully ferritic already at 1350 °C. The jaw spacing was 60 mm as this enabled good control of the temperature and reduced the risk of overshooting. To ensure that the peak temperature had been reached, the samples were evaluated in the center of the samples in proximity to the location of the thermocouples. Approximately 20 mm in the center of the sample showed a uniform microstructure indicating that full ferritization was obtained in this region.

The holding times were chosen to demonstrate the influence of the peak temperature on the microstructure but also to reveal which effect longer holding times would have on grain growth and if the ferrite content is affected. The heating followed a rate of 150 °C/s, but to avoid overshooting

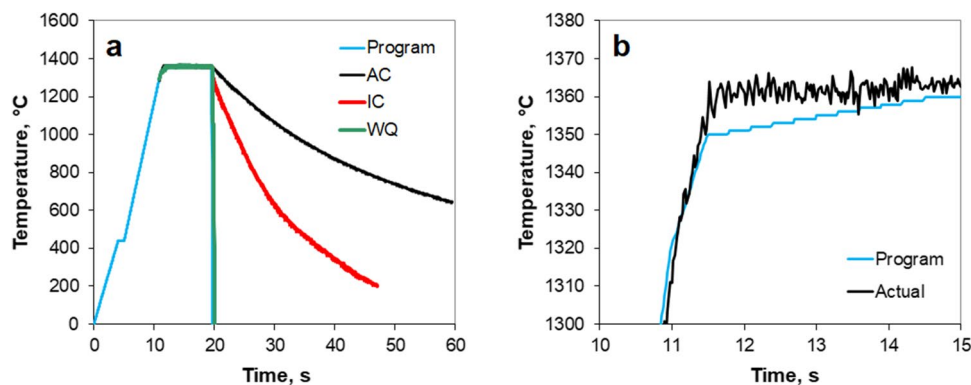


Fig. 1 Gleeble®-simulation program to reach 1360 °C where the sample was kept for 0, 5, 10, or 30 s followed by air cooling, cooling with compressed Ar, or water quenching. **a** Overview and cooling curves. The temperature was increased at a rate of 100 °C/s up to 440 °C stopping for 1 s, and then, heating occurred at a rate of 150 °C/s up

to 1320 °C. **b** Detailed view of the controlled programming to avoid overshooting the aimed temperature of 1360 °C. The heating rate was reduced to 20 °C/s from 1320 °C and 3.3 °C/s from 1350 °C up to the peak temperature 1360 °C

the target temperature of 1360 °C, the program started somewhat slower including a 1-s stop at 440 °C and the heating rate was reduced when getting closer to the aim. First, it was decreased to be 20 °C/s from 1320 to 1350 °C/s and the last 10 °C were set to take 3 s (Fig. 1b). After heating, the specimens were cooled at different rates using air cooling, compressed Ar, and water quenching down to ambient temperature. The cooling rates were estimated to be 20 °C/s, 75 °C/s, and 400 °C/s, respectively. If water was used, the chamber was dried before the next sample was mounted. Water quenching would represent the highest cooling rates obtained in laser welding and when welding thick material, while the other two cooling rates were the highest that could be obtained with the equipment available. It is challenging to measure the actual cooling rate in the HT-HAZ of real welds as this zone is very narrow. Attempts in this work showed that the maximum temperature reached 1 mm away from the fusion line was only 850 °C with a cooling rate of 70 °C/s down to 600 °C. Valiente Bermejo et al. [98] made advanced tests with harpooned thermocouples when welding UNS S32750, and at the maximum reached temperature of 750–1073 °C, the average cooling rate was 115 °C/s. Programmed step cooling would be slower and thus be irrelevant for any practical welding.

Some important observations were made when welding the thermocouples to the surface of the UNS S32101 as compared to previous experience with HT-HAZ Gleeble®-simulations of other duplex stainless steels. It was as usual beneficial to sand the outer surface of the UNS S32101 with a fine paper, but the high manganese content in the base material may have affected the weldability. It was rare that the individual thermocouples adhered to the surface at the first attempt, but if this was the case, they were intentionally removed. Otherwise, the wires often detached while ramping up the temperature and the sample had to be scrapped. As the surface of the samples exceeded 700 °C, it is possible that the manganese oxide observed in the weld oxide of UNS S32101 [99] also played a role here. Instead, a procedure was developed where the thermocouples were welded to the same spot 3–5 times to build up a larger joint.

2.5 Metallographic examination

Cross-sections of the welds and Gleeble®-simulated specimens were prepared using standard techniques to 3 µm and polished with SiO₂ in the last step. For the stationary welds, it was crucial to cut the samples with a margin and thereafter grind and polish to land at the exact center. These were for this reason prepared manually. The microstructure was elucidated with a modified Beraha II etchant (60 ml H₂O + 30 ml HCl + 0.9–1 g K₂S₂O₅) and the ferrite content measured with image analysis using the software Optimas 6.1 (Media Cybernetics, Inc., Rockville, Maryland, USA). The width of the

HT-HAZ was measured at 10 locations on micrographs taken of the cross-section. The grain size of the Gleeble®-simulated specimens was quantified as the equivalent diameter of a circular disk with the same area as the grain.

2.6 COMSOL simulation

COMSOL Multiphysics v6.0 (COMSOL Multiphysics GmbH, Göttingen, Germany) software was applied for numerical modelling using the heat transfer in solids interface. The arc was set as stationary (non-moving) and the geometry of the fusion line chosen based on actual welds in accordance with the model developed by Kumara [100].

The energy equation governs the temperature distribution in the plate. Expressed in terms of the temperature T , the energy equation reads:

$$\rho C_p \frac{\partial T}{\partial t} + \rho C_p \mathbf{u} \cdot \nabla T + \nabla \cdot \mathbf{q} = Q + Q_{\text{ted}}, \quad (1)$$

where ρ is the material density, C_p the specific heat capacity at constant pressure, \mathbf{u} the velocity vector, \mathbf{q} the conductive heat flux, Q the heat source, and Q_{ted} the thermoelastic damping. In addition to the energy equation, Fourier's law of heat conduction was used. This states that the conductive heat flux is proportional to the temperature gradient, such that

$$\mathbf{q} = -k \nabla T, \quad (2)$$

where k is the thermal conductivity of the material. The heat source and the thermoelastic damping are not considered in the present paper. The values of the density, C_p , and heat conductivity were obtained using JMatPro® (Sente Software, UK) as suggested by Vattappara et al. [101].

The material thickness was 6 mm, and for consistency with the work of Hosseini et al. [69], the width of the material was chosen to be a circular plate with a radius of 50 mm. However, analysis revealed that the spatial variation of temperature beyond horizontal distances of 10 mm was negligible. The heat source was considered as a 1-mm spot in the weld center of the weld. The model and heat transfer analysis were conducted under axi-symmetric assumptions, resulting in a two-dimensional representation (cut plane). The left boundary was designated as the symmetry axis, while room temperature was applied to the right boundary. The different weld shapes were obtained from etched cross-sections and the fusion line temperature assumed to be 1400 °C (ferrite solidus), as determined with Thermo-Calc earlier [102]. The top and bottom surfaces were assigned the same conditions as those utilized in Vattappara et al. [101], where real-time thermocouple (TC) readings were employed on the samples combined with TC measurements in a previous work [99].

3 Results

3.1 Stationary arc welds

Figure 2 displays a selection of typical cross-sections of the stationary arc welds. The weld penetration was mostly rather flat or exhibited different irregular shapes. The width of the ferritized HAZ was uneven, being wider where the shape was irregular. Higher magnifications of the HT-HAZ close to the surface are shown in Fig. 3 and the measurements of the weld shape, ferrite fraction, and nitrogen content are presented in Table 4.

Longer stationary welding time and nitrogen additions to the shielding gas resulted in wider welds. The maximum depth increased for all welds up until 20 s but was highly dependent on the weld shape, while no clear influence of the shielding gas composition could be observed. The weld metal nitrogen content increased with nitrogen additions to the shielding gas, but the extent was influenced by the stationary welding time. While the Ar welds became completely depleted in nitrogen with time, Ar + 2% N₂ resulted in a level around 0.20 wt.-%. With Ar + 5% N₂ and Ar + 8% N₂, the measured nitrogen content over time went from 0.37 to 0.21 and 0.39 to 0.25 wt.-%, respectively.

After a welding time of 0.5 s, the welds performed with Ar already showed a weld metal ferrite content of 80 vol.-%, and these became essentially fully ferritic after 10 s. The austenite content increased with nitrogen additions to the shielding gas. With Ar + 2% N₂, the average ferrite content was 68–75 vol.-% for all welds regardless of the

stationary welding time. With higher additions of nitrogen, the austenite content increased significantly, but it decreased with longer welding times. The ferrite range was 34–71 vol.-% with Ar + 5% N₂ and 32–66 vol.-% with Ar + 8% N₂. For the longest stationary welding times, the austenite precipitated mainly as intragranular and grain boundary austenite.

For the shortest welding time 0.5 s, partially transformed austenite was present all the way to the fusion line no matter which shielding gas that was used. The HT-HAZ became fully ferritic after 20 s with Ar, 60 s with Ar + 2% N₂ and 120 s for Ar + 5% N₂ and Ar + 8% N₂. For the longer stationary welding times, the welds mostly showed undercut and especially with Ar + 5% N₂ and Ar + 8% N₂. With nitrogen additions to the shielding gas, an austenite layer was found on the base material surface adjacent to the weld.

For some of the samples welded with nitrogen additions to the shielding gas, cracks were observed at the weld surface center, Fig. 4. These were located in the ferrite grain boundaries. Cracks were also observed in the HAZ and across the fusion line in one of the samples welded with Ar + 5% N₂ for 20 s, Fig. 5.

3.2 Travelling arc welds

The travelling arc welds can of the measurements are presented in Table 5. The width and depth of the welds, and the width of the HAZ increased with the arc energy. The average weld metal nitrogen content increased proportionally with the nitrogen content in the shielding gas. When using 100% Ar, nitrogen

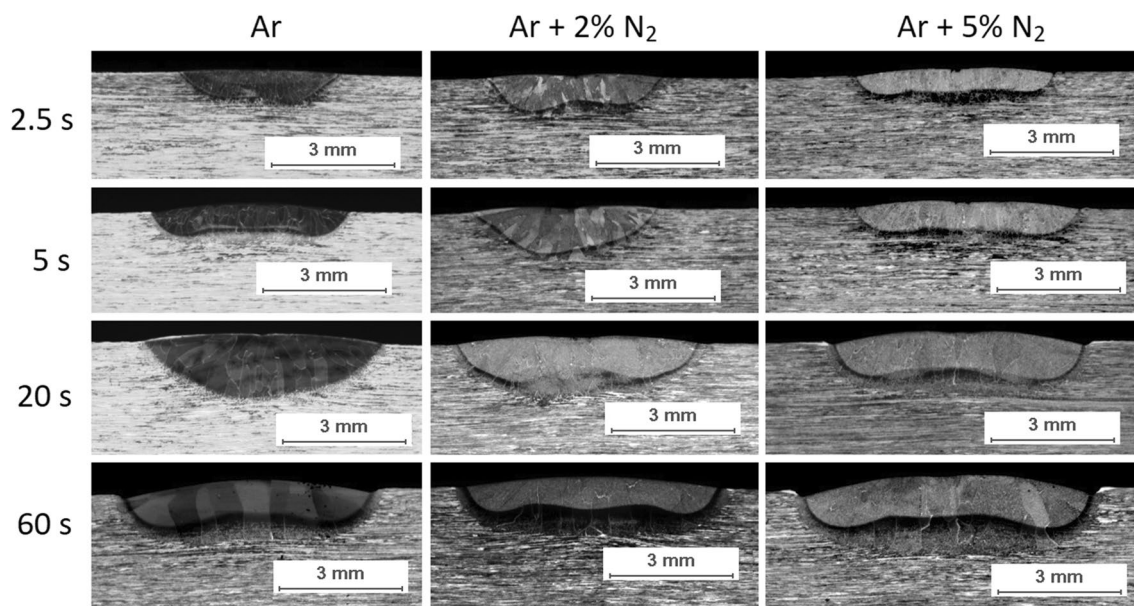


Fig. 2 Cross-sections of stationary arc welds performed with different shielding gases and welding times

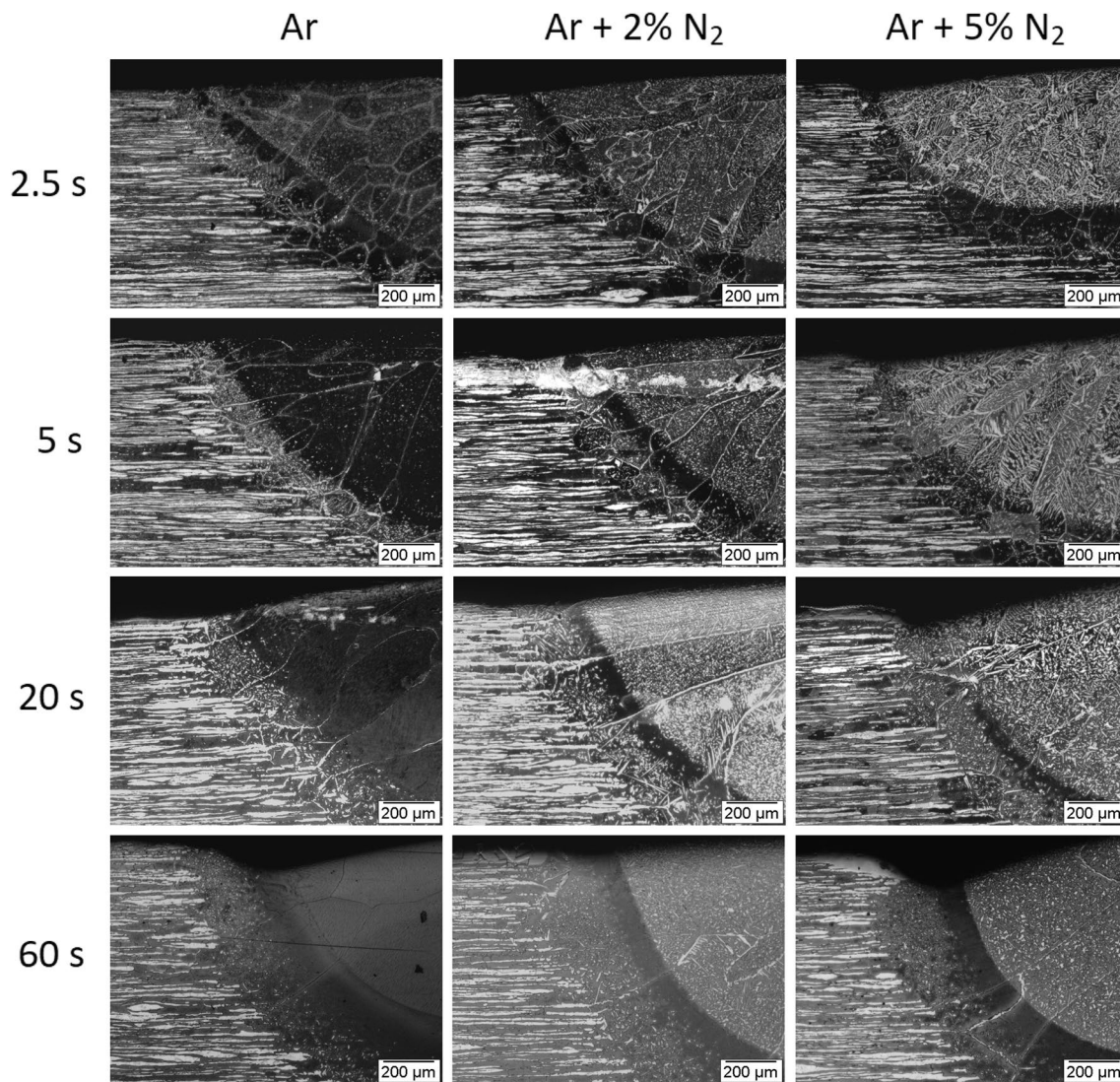


Fig. 3 Cross-sections of stationary arc welds performed with different shielding gases and welding times

loss occurred, with the depletion becoming more pronounced at higher arc energy. This phenomenon was not observed with nitrogen additions to the shielding gas, where the variation in weld metal nitrogen content was less significant. The exact location of the fusion line was not clear for all samples, and thereby, it was not possible to measure the width of the HAZ with high accuracy. With nitrogen additions, more austenite formed in the weld metal and there was an austenite layer on the surface of the weld metal and HT-HAZ (Fig. 6). Chromium nitrides were present in the weld metal and HT-HAZ, but these do not become highlighted by the Beraha II etchant used.

3.3 Gleeble® simulations

Figure 7 shows micrographs after thermo-mechanical simulation of the HT-HAZ and Table 6 the average grain size and austenite

content for each set of parameters. The grains became coarser with longer holding times at 1360 °C and smallest in the water-quenched samples. The intermediate and air-cooled samples showed significant amounts of grain boundary and intragranular and Widmanstätten austenite. After water quenching, the ferrite grains were well visible with austenite decorating the grain boundaries. Small intragranular austenite was present inside the ferrite grains, and limited amounts of Widmanstätten austenite grew into the center.

4 Discussion

4.1 Stationary arc welding

With stationary arc welding, the 100% Ar welds became almost completely depleted in nitrogen with time (Fig. 8a).

Table 4 Measured average weld metal nitrogen and ferrite content, and width and ferrite content of the HT-HAZ performed with stationary arc welding

Shielding gas	Time, s	Nitrogen content, wt.-%	Ferrite content, vol.-%		HAZ width, μm	Weld shape, mm		
			Weld metal	HT-HAZ		Diameter	Max. height	Max. depth
Ar	0.5	0.174	80 \pm 4	93 \pm 6	110 \pm 75	3.4 \pm 0.2	0.04 \pm 0.02	0.27 \pm 0.01
Ar	1	0.157	74 \pm 2	94 \pm 5	148 \pm 60	3.9 \pm 0.3	0.08 \pm 0.01	0.39 \pm 0.01
Ar	2.5	0.079	94 \pm 1	94 \pm 5	198 \pm 117	4.0 \pm 0.2	0.10 \pm 0.01	0.69 \pm 0.01
Ar	5	0.072	94 \pm 1	94 \pm 5	281 \pm 136	4.7 \pm 0.2	0.15 \pm 0.04	0.73 \pm 0.05
Ar	10	0.072	99 \pm 1	95 \pm 4	348 \pm 143	5.1 \pm 0.1	0.18 \pm 0.03	1.02 \pm 0.10
Ar	20	0.054	99 \pm 1	99 \pm 1	436 \pm 102	5.7 \pm 0.1	0.21 \pm 0.03	1.34 \pm 0.05
Ar	60	0.029	99 \pm 1	99 \pm 1	558 \pm 245	6.1 \pm 0.1	0.35 \pm 0.04	0.81 \pm 0.02
Ar	120	0.020	99 \pm 1	99 \pm 1	703 \pm 242	6.3 \pm 0.1	0.26 \pm 0.05	0.77 \pm 0.04
Ar+2% N ₂	0.5	0.207	69 \pm 2	85 \pm 12	109 \pm 75	3.3 \pm 0.1	0.07 \pm 0.01	0.53 \pm 0.04
Ar+2% N ₂	1	0.207	67 \pm 2	88 \pm 11	117 \pm 60	3.6 \pm 0.1	0.08 \pm 0.01	0.54 \pm 0.01
Ar+2% N ₂	2.5	0.207	73 \pm 4	94 \pm 5	164 \pm 94	4.1 \pm 0.2	0.10 \pm 0.01	0.77 \pm 0.01
Ar+2% N ₂	5	0.203	75 \pm 3	94 \pm 9	214 \pm 98	4.4 \pm 0.1	0.12 \pm 0.01	1.00 \pm 0.01
Ar+2% N ₂	10	0.187	71 \pm 5	94 \pm 3	260 \pm 131	4.9 \pm 0.1	0.19 \pm 0.01	1.03 \pm 0.01
Ar+2% N ₂	20	0.216	68 \pm 3	95 \pm 3	411 \pm 137	5.7 \pm 0.2	0.23 \pm 0.04	1.05 \pm 0.05
Ar+2% N ₂	60	0.186	68 \pm 3	99 \pm 1	510 \pm 210	6.2 \pm 0.8	0.24 \pm 0.01	0.90 \pm 0.06
Ar+2% N ₂	120	0.176	70 \pm 6	99 \pm 1	658 \pm 188	6.6 \pm 0.2	0.31 \pm 0.01	0.79 \pm 0.10
Ar+5% N ₂	0.5	0.369	34 \pm 7	88 \pm 11	99 \pm 88	3.8 \pm 0.1	0.08 \pm 0.01	0.29 \pm 0.02
Ar+5% N ₂	1	0.353	39 \pm 4	89 \pm 11	131 \pm 90	4.2 \pm 0.1	0.12 \pm 0.01	0.39 \pm 0.01
Ar+5% N ₂	2.5	0.310	48 \pm 3	90 \pm 6	152 \pm 116	4.8 \pm 0.1	0.15 \pm 0.01	0.46 \pm 0.01
Ar+5% N ₂	5	0.293	55 \pm 4	89 \pm 2	220 \pm 139	5.4 \pm 0.1	0.19 \pm 0.01	0.60 \pm 0.02
Ar+5% N ₂	10	0.296	56 \pm 4	93 \pm 3	257 \pm 153	5.4 \pm 0.2	0.25 \pm 0.02	0.62 \pm 0.08
Ar+5% N ₂	20	0.260	61 \pm 3	94 \pm 2	389 \pm 189	6.0 \pm 0.1	0.27 \pm 0.01	0.85 \pm 0.08
Ar+5% N ₂	60	0.213	68 \pm 3	99 \pm 1	471 \pm 343	6.7 \pm 0.2	0.42 \pm 0.04	0.87 \pm 0.06
Ar+5% N ₂	120	0.208	71 \pm 4	99 \pm 1	635 \pm 211	6.8 \pm 0.3	0.42 \pm 0.04	0.69 \pm 0.08
Ar+8% N ₂	0.5	0.387	32 \pm 7	90 \pm 9	94 \pm 76	3.8 \pm 0.5	0.08 \pm 0.01	0.35 \pm 0.01
Ar+8% N ₂	1	0.347	37 \pm 4	93 \pm 4	131 \pm 94	4.1 \pm 0.1	0.09 \pm 0.01	0.42 \pm 0.01
Ar+8% N ₂	2.5	0.343	45 \pm 2	92 \pm 11	162 \pm 119	4.7 \pm 0.1	0.12 \pm 0.01	0.67 \pm 0.02
Ar+8% N ₂	5	0.329	49 \pm 4	94 \pm 3	233 \pm 165	4.9 \pm 0.1	0.13 \pm 0.02	0.71 \pm 0.02
Ar+8% N ₂	10	0.333	50 \pm 2	92 \pm 3	268 \pm 167	5.9 \pm 0.1	0.21 \pm 0.01	0.76 \pm 0.01
Ar+8% N ₂	20	0.300	55 \pm 2	93 \pm 4	366 \pm 221	6.6 \pm 0.1	0.23 \pm 0.01	0.79 \pm 0.02
Ar+8% N ₂	60	0.258	63 \pm 5	98 \pm 2	465 \pm 201	6.9 \pm 0.1	0.33 \pm 0.02	0.89 \pm 0.04
Ar+8% N ₂	120	0.247	66 \pm 2	99 \pm 1	595 \pm 147	6.9 \pm 0.1	0.24 \pm 0.04	0.96 \pm 0.04

The weld metal nitrogen content increased with nitrogen additions to the shielding gas but decreased over time. The only exception was Ar+2% N₂, where the nitrogen level remained relatively stable at 0.199 \pm 0.013 wt.-%, slightly below the base material at 0.226 wt.-%. With Ar+5% N₂ and Ar+8% N₂, the measured nitrogen content decreased over time from 0.37 to 0.21 and 0.39 to 0.25 wt.-%, respectively. This suggests that, after a certain duration, the nitrogen solubility with all gases containing nitrogen additions approached the level of the parent material.

The weld metal austenite content decreased with stationary welding time for all shielding gases, except for Ar+2% N₂ (Fig. 8b). With Ar, the welds rapidly became fully ferritic, while all nitrogen-containing shielding gases resulted in

approximately 70 vol.-% ferrite after 20–120 s. This indicates that the weld metal composition and resulting nitrogen solubility may reach a steady state at longer durations. The general ferritization would probably be connected to the partially time-dependent element loss from the weld metal reported in an earlier work [99]. Primarily manganese and nitrogen evaporate and can be found after subsequent deposition in the weld oxide formed on duplex alloys [103]. This is supported by the undercut in the fusion line and the austenite layer observed on the base material surface of samples subjected to longer welding times. Welds with undercut have also been observed with the arc heat treatment method [89, 101].

The irregular weld shape, characterized with large variations in the HAZ, led to a significant standard deviation. On

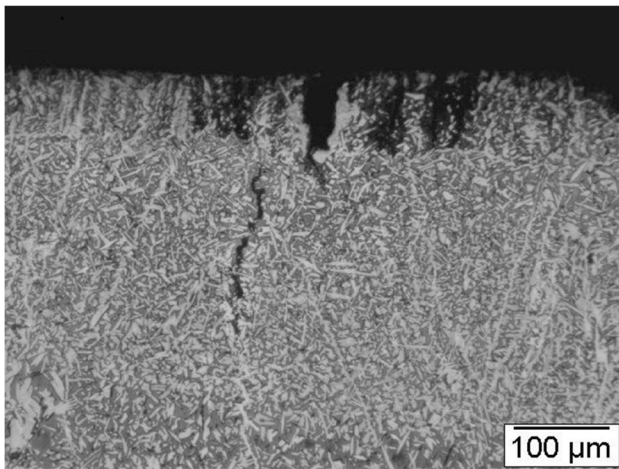


Fig. 4 Stationary arc welds with cracks observed at the surface of a sample welded with Ar + 5% N₂ for 1 s

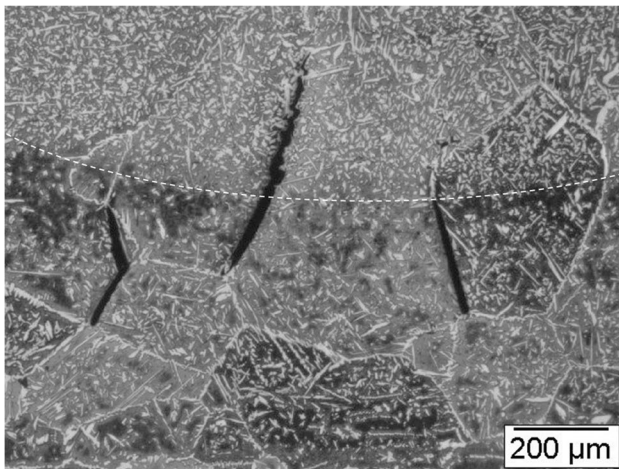


Fig. 5 Cracks observed in the HAZ and across the fusion line (indicated) of a stationary arc weld performed with Ar + 5% N₂ for 20 s

average, the weld width increased with the welding time and the widest HAZ was observed when welding with Ar (Fig. 8c). This is suggested to be the result of faster nitrogen depletion in the weld metal with Ar than with the other gases. Considerable nitrogen loss from the weld metal would be followed by enhanced nitrogen diffusion from the HT-HAZ and faster ferritization. A small reduction of the HAZ width could be observed with higher nitrogen additions. For the shortest stationary arc welding times, the ferrite content in the HAZ was highest for Ar but generally increased for all shielding gases with time. In all, this supports that some nitrogen loss eventually took place in the HT-HAZ although nitrogen was added to the shielding gas. It should be noted that the austenite reformation is also highly dependent on the cooling rate. As only up to 1/8 of the 6-mm-thick plate was penetrated, the cooling was rapid.

The weld metal width increased with the nitrogen content in the shielding gas and the stationary arc welding time (Fig. 8d), but the same relationship could not be seen for the weld penetration and height. Nitrogen increased the voltage indicating that the arc energy was higher.

For examination and simulation of the HT-HAZ, it appears that the stationary arc welding method has almost no relevance regardless of shielding gas type. This is suggested to be the result of the stationary condition leading to longer time spent in the fully ferritic region. The HAZ was completely different from the real arc welds with an uneven shape, substantially wider width, and more ferrite in the center root part. The band of fully ferritic structure appeared somewhat earlier with Ar and became slightly wider, but after 120 s, the HT-HAZs produced with all shielding gas types were visually more or less identical.

4.2 Comparison of stationary arc welding and arc heat treatment

Cederberg et al. [91] simulated additive manufacturing of super duplex stainless steel by arc heat treatment of 6-mm-thick material in different ways for a total of 5–75 s. UNS S32750 was welded using the gas metal arc welding (GMAW) process with Ar as shielding gas and an ER2509 type wire with 0.22 wt.-% nitrogen. After 5 s of arc heat treatment, the width of the HT-HAZ was around 220 μm, which was in agreement with the results here for UNS S32101. However, after 75 s, the maximum width of 1 mm was approximately 40% wider than after 120 s of stationary arc welding on UNS S32101. The accelerated ferritization might be attributed to a lower nitrogen content in the built-up material. After 5 s, the weld was wider and shallower than what could be seen here for UNS S32101, but the width did not increase as rapidly with longer welding times. None of the welds became as deep as in UNS S32101, and longer arc heat treatment did not influence the depth. In addition to differences in chemical composition, it is worth noting that the arc heat treatment was conducted at slightly higher current and water cooling was consistently applied on the root side.

Just as observed with the arc heat treatment method developed by Hosseini et al. [69], the long stationary arc times deplete the weld metal and HT-HAZ of nitrogen. None of the methods is thus representative for real welds. The arc heat treatment may, however, be useful for creating TTT diagrams and for studying particles formed at lower temperatures (LT-HAZ) [46, 88–91].

4.3 Hot cracking in stationary arc welds

The surface center cracks in Fig. 4 could naturally be the effect of shrinkage similar to that of casting and crater pipe cracks but were here only observed for the welds performed with nitrogen

Table 5 Travelling arc welds performed with four different shielding gases and various heat inputs

Shielding gas	Arc energy, kJ/mm	Ferrite content, vol.-%		HAZ width, μm	Nitrogen LECO, wt.-%	Weld shape, mm		
		Weld metal	HT-HAZ			Width	Depth	Height
Ar	0.38	73 \pm 1	75 \pm 4	180 \pm 28	0.172	3.55	0.65	0.10
Ar	0.48	82 \pm 2	81 \pm 5	172 \pm 18	0.146	3.40	0.73	0.08
Ar	0.57	80 \pm 2	79 \pm 4	228 \pm 43	0.150	4.01	0.83	0.13
Ar	0.67	82 \pm 4	81 \pm 6	260 \pm 24	0.147	4.56	0.96	0.15
Ar	0.87	86 \pm 4	85 \pm 7	273 \pm 34	0.119	4.86	1.12	0.17
Ar	0.96	90 \pm 4	84 \pm 5	296 \pm 53	0.135	4.15	0.96	0.17
Ar	1.19	89 \pm 2	87 \pm 7	369 \pm 64	0.106	5.11	1.43	0.21
Ar+2% N ₂	0.43	69 \pm 4	79 \pm 5	178 \pm 35	0.197	3.44	0.72	0.13
Ar+2% N ₂	0.52	61 \pm 2	75 \pm 6	196 \pm 33	0.240	3.91	0.51	0.12
Ar+2% N ₂	0.63	69 \pm 2	72 \pm 5	244 \pm 34	0.206	4.43	0.88	0.12
Ar+2% N ₂	0.88	71 \pm 1	74 \pm 4	276 \pm 88	0.194	4.21	1.09	0.19
Ar+2% N ₂	0.90	76 \pm 2	78 \pm 3	280 \pm 62	0.196	4.95	1.21	0.19
Ar+2% N ₂	1.00	73 \pm 2	77 \pm 5	286 \pm 45	0.184	5.23	1.34	0.20
Ar+2% N ₂	1.20	75 \pm 3	78 \pm 4	360 \pm 85	0.183	5.53	1.74	0.19
Ar+5% N ₂	0.50	66 \pm 2	73 \pm 8	180 \pm 42	0.248	3.77	0.97	0.12
Ar+5% N ₂	0.96	66 \pm 3	76 \pm 4	240 \pm 32	0.247	4.45	1.33	0.17
Ar+8% N ₂	0.55	64 \pm 3	74 \pm 5	203 \pm 45	0.262	3.88	0.82	0.15
Ar+8% N ₂	0.93	61 \pm 2	75 \pm 6	271 \pm 51	0.278	4.46	1.27	0.16

in the shielding gas. The combination of nitrogen additions and stationary arc welding possibly created oversaturation of nitrogen and excessive local formation of austenite. This could cause primary austenitic solidification and hot cracking similar to that seen for fully austenitic stainless steel welds [104, 105]. Examination in as-polished condition ruled out that it was an etching effect. No specific relationship could be seen between the welding time and the amount of nitrogen in the shielding gas. Cracks were found after 1 s with Ar+5% N₂, after 20 s with Ar+2% N₂, and 60 s with Ar+2% N₂ and Ar+8% N₂. It cannot be excluded that the phenomenon is related to formation of “false nitrogenous pearlite” [106–108], which occasionally is also found for hyper duplex UNS S32906 welded with nitrogen in the shielding gas [109]. In addition, it has been shown that the manganese content decreases with both the nitrogen content and stationary welding time [99]. This may be of importance as manganese can improve the resistance to hot cracking.

One of the samples performed with Ar+5% N₂ for 20 s also showed cracks in the HT-HAZ and across the fusion line. These are rather suspected to be caused by liquation of low-melting phases in grain boundaries such as sulfur, phosphorous, and boron. None of these hot cracking phenomena was observed for the travelling arc welds, which underlines the difference between the stationary and travelling arc welds.

4.4 Travelling arc welding

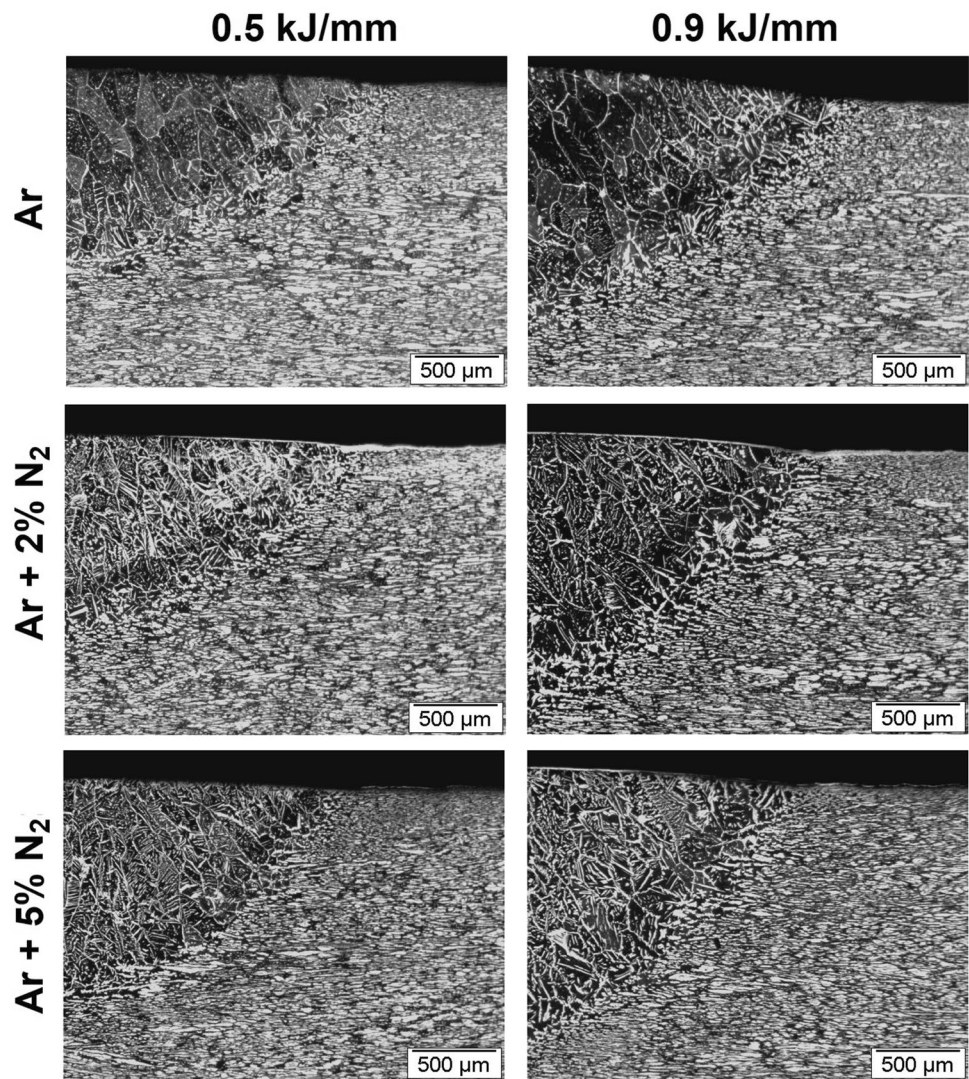
Due to its effect on the thermal cycle, the arc energy can have a significant influence on the structure and properties of

welded duplex stainless steels. High heat inputs (low cooling rates) are generally avoided to prevent excessive ferrite grain growth, unnecessary dilution, and formation of intermetallic phases in primarily super duplex grades [11]. Conversely, too low heat inputs (rapid cooling rates) could result in insufficient time for adequate austenite formation. This can lead to highly ferritic microstructures and considerable nitride precipitation within the ferrite grains in the HAZ and fusion zone, which negatively affects the corrosion resistance and toughness [16, 67].

For the travelling arc welds performed with different shielding gases and arc energies ranging from 0.4 to 1.2 kJ/mm, certain observations were made. The weld width, penetration, and height increased with the heat input. This is consistent with previous results in the work of Gupta et al. [110]. There were no additional effects observed with nitrogen additions to the shielding gas, but there was a general increase in both weld metal nitrogen content and austenite formation. With Ar+2% N₂, the nitrogen loss with higher arc energy was so small that it was almost negligible, and hence, no noteworthy increase in ferrite content could be confirmed. Likewise, there was no apparent relationship between nitrogen content and austenite formation with the arc energy for either Ar+5% N₂ or Ar+8% N₂. Ar exhibited some weld metal nitrogen loss and a slight increase in ferrite fraction with higher arc energy, which aligns with previous studies [29, 110, 111].

In the HAZ, the ferrite content increased with the arc energy for the welds welded with Ar as shielding gas, but

Fig. 6 Example of travelling arc welds performed with three different shielding gases and two different arc energies



not for welds with nitrogen additions. This indicates some nitrogen loss from the HT-HAZ to the weld metal when using Ar. For the welds performed with nitrogen additions to the shielding gas, more austenite formed in the HAZ, but this could not be correlated to the amount of nitrogen in the shielding gas nor the heat input. Similar observations have also been made for UNS S32304 and UNS S32750 [112]. Increasing the heat input above 3 kJ/mm may enhance austenite formation in the HT-HAZ, but it may come at the cost of reduced impact toughness [113]. In multipass welding, the subsequent weld passes may affect the HAZ morphology. However, the present work only takes single bead welding into consideration and is thereby not considering any reheating of the HAZ.

4.5 Fluid mechanics

The initial shape of the stationary arc welds was wide and shallow, indicating that the flow in the melt goes

primarily outwards. With time, the welds became wider, with the deepest part being the sides, forming an uneven shape. For the shielding gases containing nitrogen, the center of the weld became deeper with time. This appeared when the weld had reached a width of approximately 6.6 mm, which took 120 s with Ar + 2% N₂, 60 s with Ar + 5% N₂, and 20 s with Ar + 8% N₂. Nitrogen additions to the shielding gas make the arc hotter as indicated by the higher voltage in Table 2.

In full penetration welding, the width of the melt has been reported to initially increase rapidly until the heat conduction from the base metal considerably slows down the process [114]. Once this stage has been reached, the Marangoni flow would become more pronounced and the penetration depth increase. The Marangoni effect could not be observed for the stationary arc welds, which could possibly be related to the rapid cooling from the relatively thick plate and low sulfur content in the parent material.

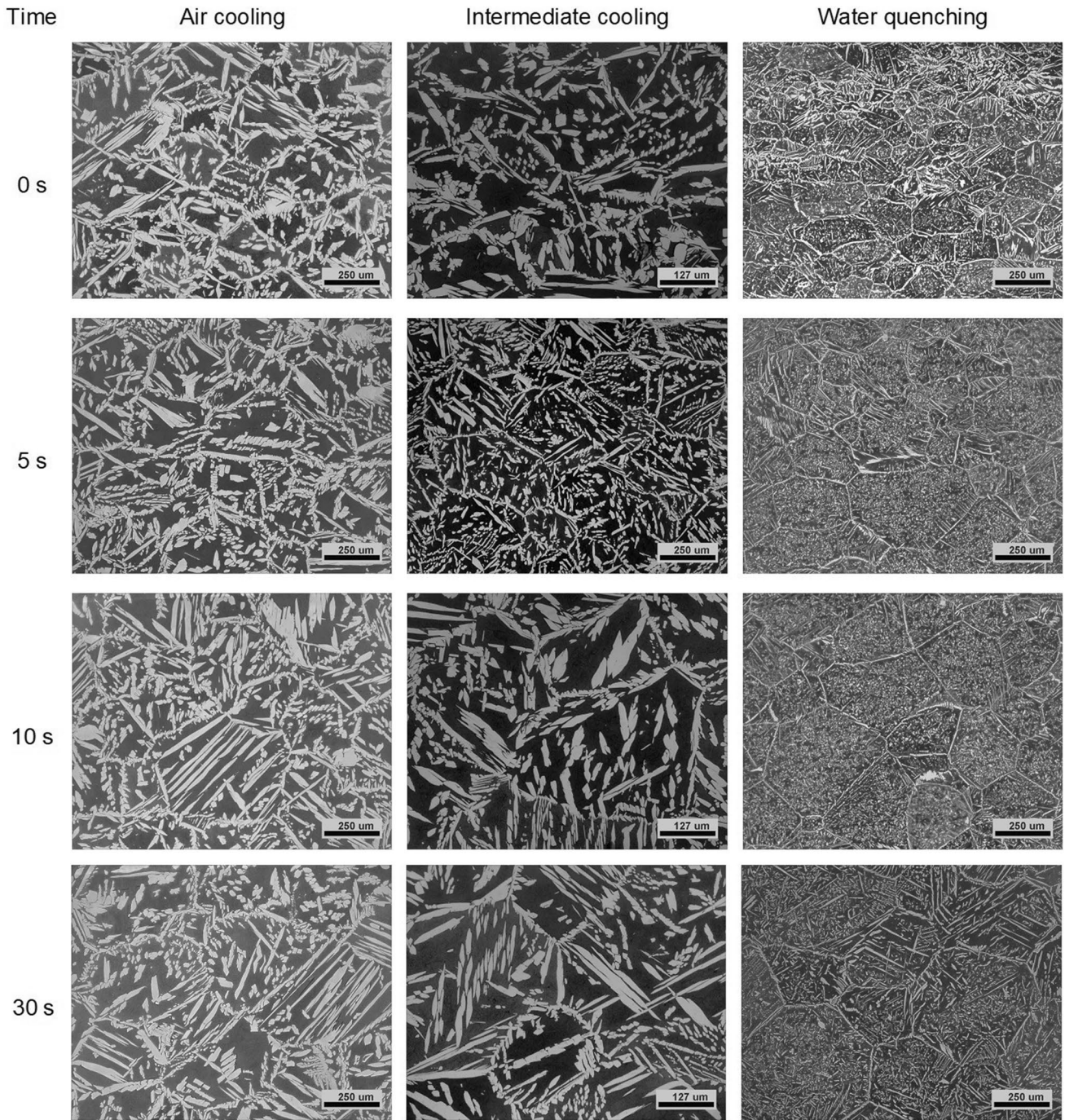


Fig. 7 Gleeble[®]-simulated HT-HAZ microstructures at different holding times and cooling rates (two scales)

4.6 Thermal simulation of known weld shapes

Figure 9 illustrates the temperature distribution and isothermal lines for three stationary arc weld geometries and one travelling arc weld. Figure 9a and b indicate that the warmest section would be in the center, where also the widest HT-HAZ could be observed. Figure 9c shows

that the highest temperatures would be obtained where the most uneven shapes were observed, which also could be confirmed in the etched cross-sections. Figure 9d shows the temperature distribution in the cross-section of a travelling arc weld performed with an arc energy of 0.4 kJ/mm. Here, the temperature profile was narrower and more uniform with a slightly higher concentration in

Table 6 Measured grain size and austenite content for the Gleeble[®]-simulated HT-HAZ. The ferrite content of the base material was $53 \pm 6\%$

Peak temperature, °C	Time, s	Cooling, °C/s	Grain size, μm	Ferrite, vol.-%
1360	0	400	131 ± 25	75 ± 5
1360	5	400	194 ± 30	82 ± 5
1360	10	400	253 ± 41	80 ± 6
1360	30	400	415 ± 92	75 ± 4
1360	0	75	169 ± 14	63 ± 2
1360	5	75	214 ± 36	62 ± 2
1360	10	75	303 ± 40	62 ± 2
1360	30	75	461 ± 117	63 ± 2
1360	0	20	204 ± 29	59 ± 2
1360	5	20	249 ± 24	61 ± 2
1360	10	20	331 ± 48	59 ± 2
1360	30	20	459 ± 96	60 ± 1

the deepest section. This also matched the actual situation well.

For the stationary arc welds, the model predicted that the HT-HAZ would be wider at the surface than what could be observed in reality. It should be noted that this problem inherently exhibits a strong dependence on time as the shape of the weld is contingent upon the duration of the heat source (arc) acting upon the material. Especially the width increased with time for the stationary arc welds. However, in the present computational study, the temporal evolution of the fusion zone shape has not been incorporated. Instead, the focus lies on analyzing the temperature distribution for a fixed shape, considering the prescribed boundary temperatures.

It is important to note that the current model does not consider the phase transition from solid to liquid (including potential nitrogen diffusion from the HT-HAZ to the weld metal) and the comprehensive history of temperature during the welding process is not accounted for. This simplification was deliberately implemented to primarily

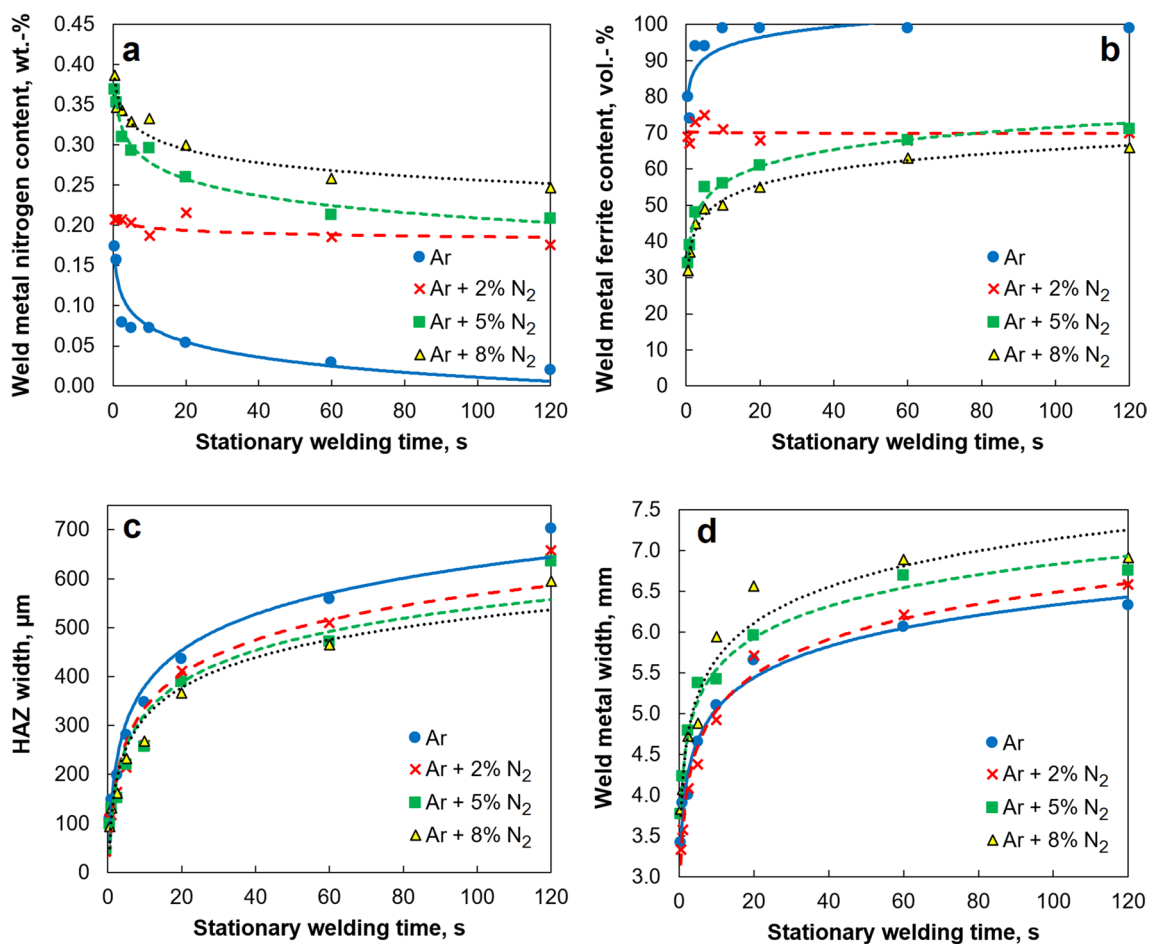


Fig. 8 Effect of shielding gas composition and stationary arc welding time on the average **a** weld metal nitrogen content, **b** weld metal ferrite content, **c** HAZ width, and **d** weld metal width

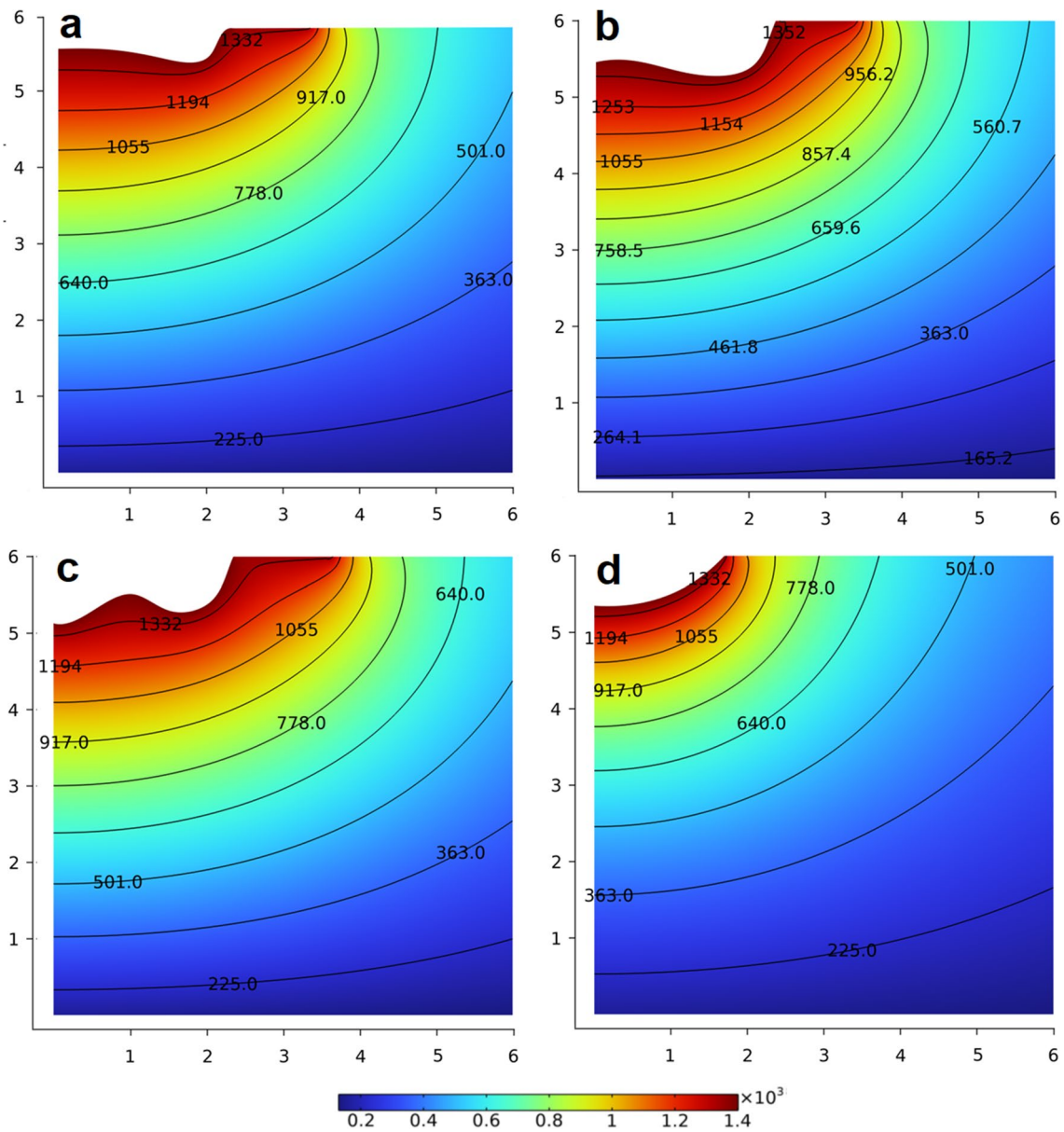


Fig. 9 Temperature distribution—surface plot (color scheme) and contour plot showing isothermal lines. Stationary welding with **a** Ar+8% N₂ for 2.5 s, **b** Ar for 60 s, **c** Ar+8% N₂ for 60 s, and **d**

travelling arc welding with Ar with an arc energy of 0.4 kJ/mm. All temperatures are given in °C and dimensions in mm

highlight the disparities in temperature distribution among different weld geometries for stationary arc welding as compared to travelling arc welds, while considering the specified boundary conditions.

The primary temperature distribution pattern remained largely unchanged despite variations in the shape of the fusion zone. The principal distinction lies in the temperature distribution near the boundary of the fusion line, as evidenced by the alterations in the configuration of the isothermal lines corresponding to the specific zone shape. However, as one moves a short distance away from the

fusion zone boundary, the temperature distribution converges to a nearly identical pattern. This convergence is further illustrated by the nearly indistinguishable shapes of the isothermal lines.

4.7 Gleeble® simulation

At the peak temperature 1360 °C, the material became fully ferritic, and the grain size increased with the holding time. Water quenching with rapid cooling resulted in the smallest grains, while the grains grew slightly larger with the slower

cooling obtained with compressed Ar and air cooling. The influence of the cooling rate became less pronounced with longer holding times. At the shorter holding times, more partially transformed austenite remained in some of the samples, which is expected to have pinned the grain boundaries and prevented grain growth as described by Atamert and King [41]. Thus, once the partially transformed austenite was completely dissolved, the differences between the samples became smaller.

The ferrite content was not found to be affected by the increased holding time, but clearly by the cooling rate. No significant loss of nitrogen could be confirmed as compared to the actual welds and especially the stationary arc welds. This may be explained by the absence of fusion line and melt in the simulated HT-HAZ. The austenite reformation was undoubtedly lowest for the water-quenched samples. Visually the difference was small between the slower cooled samples and the average austenite content did not significantly increase further with air cooling. This could be due to further grain growth at slower cooling rates, which leads to greater distances over which the alloy elements must diffuse [115]. As expected, the intermediate and air-cooled samples showed both coarser grain boundary and intragranular austenite and considerably more Widmanstätten austenite than with rapid cooling [86]. The individual grains were thus not as easily visible as for the water quenched samples where the grain boundary austenite was thinner.

The simulated microstructures were mostly homogenous and could be reliably tested as concluded by Adonyi [116]. However, a few questionable samples were observed. The presence of banded structures after shorter (Fig. 10a) or longer holding times (Fig. 10b) indicated that the center had not reached the target temperature of 1360 °C, leading to exclusion of these samples from the evaluation. This type of centerline segregation is normal in high-alloyed stainless steels. The reason why it only remained in a few samples remains unclear, as the surrounding grains matched those observed in the other samples. This type of appearance would be even more critical for evaluating the impact toughness [22, 81].

No other phases or intermetallics were found with the etchant used. However, the ferrite grain centers contained chromium nitrides of Cr_2N type, and carbides were observed in the grain boundaries, as shown in previous work using transmission electron microscopy (TEM) on carbon replicas [81].

4.8 Evaluation of methods for HT-HAZ simulation

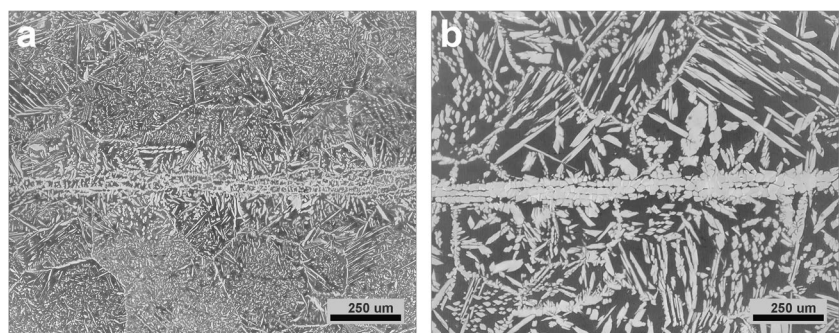
4.8.1 Shape of weldment

The shape of the stationary arc welds was not semi-circular as for the travelling arc welds, but rather flat or irregular (Fig. 2). This is most probably an effect of convection in the molten metal. Depending on the shielding gas type, the width and height of the stationary arc welds performed with the shortest welding times were in reasonable agreement with the travelling arc welds. However, the maximum depth measured with higher arc energies could not be reached with any of the stationary arc welding times. The travelling arc welds were generally deeper than what could be measured for the stationary welds, and this is suspected to be related to the difference in shape and less evaporation of alloying elements.

4.8.2 Weld metal nitrogen content

Differences were observed in the weld metal nitrogen content between the stationary and travelling arc welds. If the arc was not moving, there was a nitrogen loss with longer welding times for all shielding gases except Ar + 2% N_2 . When the arc moved, only Ar showed additional nitrogen loss with higher arc energy. For stationary arc welding with Ar, only the shortest welding times (0.5 and 1 s) resulted in values in the same range as for the travelling arc welds. Already after 2.5 s, the values were below that of the highest arc energy applied in travelling arc welding. With both Ar + 5% N_2 and Ar + 8% N_2 , the stationary arc welds absorbed considerably more nitrogen than the travelling arc welds and over 20 s were needed to reach the same level in the weld metal as for the travelling arc welds.

Fig. 10 Banded structure remaining in the center of **a** sample water quenched after 5 s and **b** sample air cooled after 30-s holding time



4.8.3 Weld metal ferrite content

As could be expected based on the nitrogen measurements, deviations could also be observed when comparing the austenite formation in the weld metal. For the stationary arc welds performed with Ar, the weld metal austenite formation after 0.5 and 1 s were in the same range as for the travelling arc welds. Already after 2.5 s, the average ferrite content was 94 vol.-%. Such low austenite formation capability was not seen for any of the actual bead-on-plate welds, where the weld metal ferrite content range was 73–90 vol.-%. After 10 s, the Ar welds had reached complete ferritization and it became difficult to locate the fusion line. The low austenite formation is a direct effect of nitrogen loss. With Ar, the method using a stationary arc only appears to be accurate for very short welding times (up to 1 s), but then the weld size is rather small, which complicates further analysis.

With Ar + 2% N₂, the austenite formation was rather similar for both processes, which would be in agreement with the fairly constant nitrogen contents. With Ar + 5% N₂, the austenite formation more than doubled as compared to the travelling arc welds. With longer stationary welding time, the austenite content decreased but over 20 s were needed to reach the same level as measured for the travelling arc welds. With Ar + 8% N₂, the situation was similar, but more than 60 s were required before the ferrite content had sunk to the same level as for the travelling arc welds. Stationary arc welding would thus not be useful for studying the effect of nitrogen additions on the weld metal austenite formation.

4.8.4 Nitrogen loss from HAZ

The EPMA mapping of the nitrogen distribution in the cross-sections of the travelling arc welds performed with an arc energy of 0.4 kJ/mm did not conclusively indicate uniform nitrogen loss in the HT-HAZ. The width of the HT-HAZ was around 100 μm, which is in agreement of the diffusion distance of nitrogen [25, 47]. The expected grain growth in the HT-HAZ was visible as the nitrogen is highly concentrated in the austenite. However, the total nitrogen content did not consistently decrease as compared to the stationary arc welds. Previous research has reported depletion of manganese, nickel, silicon, and molybdenum along the fusion line for the same material [49].

4.8.5 HAZ width

The shortest stationary arc welding times 0.5 and 1 s generally resulted in narrow HAZ widths, which could not be replicated with travelling arc welding or with any of the Gleeble® simulation parameters. The HAZ widths measured with an arc energy of 0.4–1.2 kJ/mm for the travelling arc welds were roughly similar to those observed for 2.5–10 s of stationary arc welding.

Assuming that the HT-HAZ on average consists of 1.5 grains (as suggested by Lippold et al. [73]) and that the cooling rate in the bead-on-plate welding is rapid (400 °C/s), the growth after 0–10 s of holding time in the Gleeble® matched the HAZ of the travelling arc welds with 0.4–1.2 kJ/mm and consequently also the Ar stationary arc welds for 2.5–10 s. At longer holding times, the HAZ grew significantly wider in the thermo-mechanical simulations than with stationary arc welding. Depending on the cooling rate, the HAZ width corresponding to a 1.5 × grain size obtained after 30 s holding time at 1360 °C matched the width measured for stationary welding times of 60–120 s. During welding, the HAZ grows from the fusion line in the same direction as the weld metal widens with time. Contrary, the uniform heating of the Gleeble® samples lead to three-dimensional grain growth and the grains do not become consumed by any molten weld metal. Thus, the effect of nitrogen loss from the HT-HAZ and subsequent ferritization cannot be replicated. The simulated HT-HAZ does in addition not reach as high temperatures as the actual HT-HAZ.

Lindblom et al. [80] showed that the grain size is of the same magnitude both in the real and the simulated HAZ but concluded that it can be challenging to measure the grain size in the actual HAZ due to the peak temperature gradients. This was particularly true for the travelling arc welds here where the fusion line was difficult to locate with certainty. UNS S32101 has previously been reported to have such rapid austenite formation that the fusion line can be concealed [49]. Due to the difficulties determining the exact location, the effect on the HAZ width could not be determined with absolute accuracy. For the stationary welds, the HAZ width was in addition uneven causing significant standard deviation. Measurements of the HAZ width thus remain challenging regardless of which method that is used.

4.8.6 Austenite reformation in HAZ

The stationary arc welds performed with Ar as shielding gas showed 93–99 vol.-% ferrite in the HAZ. This condition could not be confirmed for the Ar travelling arc welds where the ferrite content was 75–87 vol.-%. While having a significant effect on the austenite formation in the weld metal, nitrogen additions had less influence on the HT-HAZ. The travelling arc welds performed with nitrogen showed values of 72–79 vol.-%, while the stationary welds resulted in 85–99 vol.-%. In the latter, the HT-HAZ would be subjected to more time above the ferrite solvus temperature resulting in grain growth and more nitrogen loss to the weld metal.

The ferrite content in the HT-HAZ Gleeble® simulations was 59–82 vol.-%, while the actual bead-on-plate welds on the same heat exhibited 72–87 vol.-%. These findings align with previous reports in the literature. Hosseini and Karlsson [46] performed bead-on-plate welding using the GTAW process on 6 mm UNS S32750. They reported that the ferrite

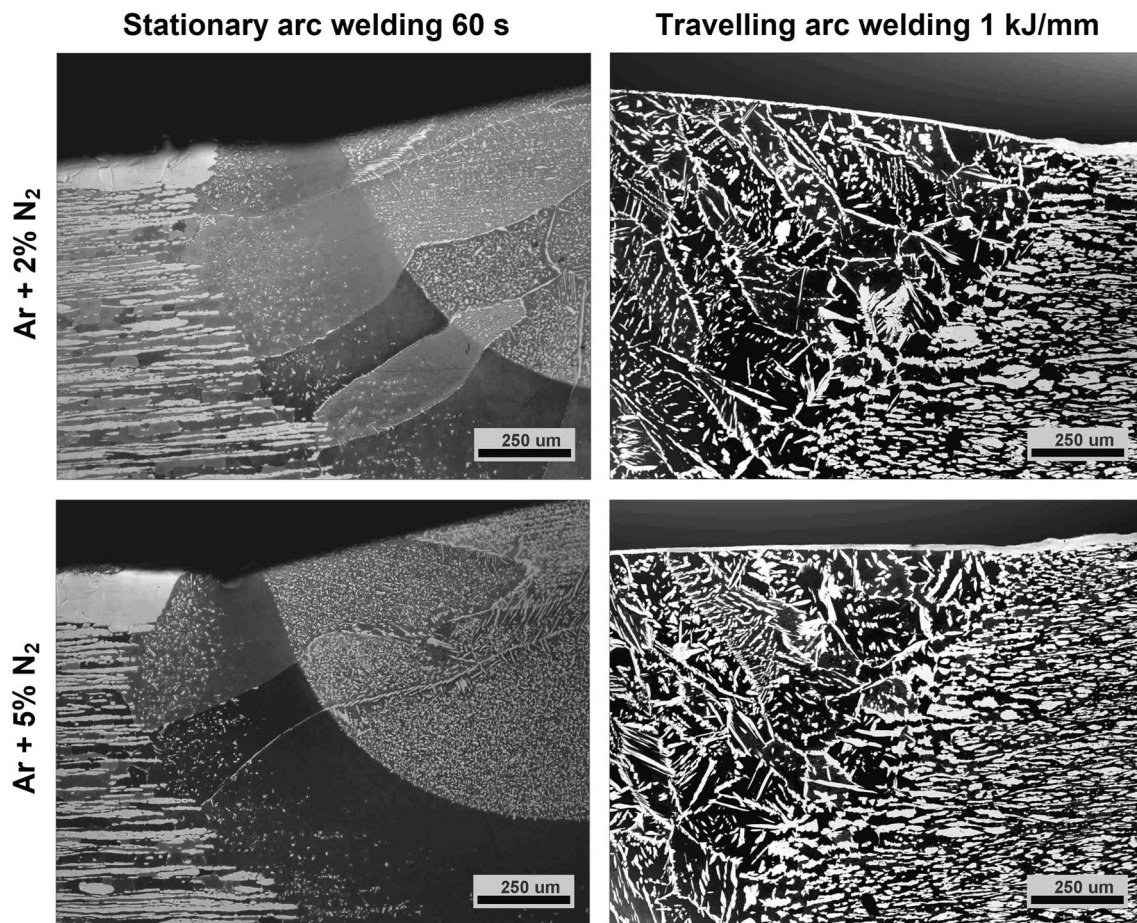


Fig. 11 Surface austenite layer formation in the HAZ of stationary and travelling arc welds

fraction in the actual HT-HAZ was 7 vol.-% higher than in the simulated HT-HAZ [46]. Similar results have been found for UNS S32205 [28] and UNS S31803 [24]. Hsieh et al. [24] observed that Gleeble[®]-simulated HT-HAZs contained about 3–6 vol.-% more austenite than in submerged arc welds on the same alloys and concluded that this is because the peak temperature reached in the simulation is somewhat lower than that of the HT-HAZ adjacent to the fusion line. This is of importance since the ferritization temperature range for modern duplex stainless steels is rather narrow [81]. Rapid cooling can be assumed as the thin welds with a measured maximum depth of 0.5–1.7 mm only reached 8–28% total penetration of the 6 mm thick plate. The highest cooling rates obtained with water quenching in the Gleeble[®] simulation here, 75–82 vol.-%, would match the ferrite fraction in the travelling arc welds fairly well (72–87 vol.-%), while the stationary arc welds resulted in 85–99 vol.-% ferrite. The thermo-mechanical simulation thus appears to be the method that comes the closest to the reality. It must be emphasized, however, that this only applies if the correct peak temperature has been reached.

4.8.7 Formation of weld surface austenite layer

With nitrogen additions to the shielding gas, the travelling arc welds formed an austenite layer covering the weld metal, HT-HAZ, and parts of the base material (Fig. 11). In contrast, when using stationary arc welding, an austenite layer was only observed on the base material. This is of importance, since the layer of austenite formed with nitrogen additions serves as a protection of the nitride-rich HT-HAZ region to pitting corrosion [117–119].

Another important observation is that the austenite formed in the stationary arc welds was present in the grain boundaries and intragranularly, but rarely as Widmanstätten austenite. In the travelling arc welds, however, Widmanstätten austenite was always found for the welds performed with nitrogen additions to the shielding gas. Longer durations of stationary arc welding contribute to ferritization in the HT-HAZ, leading to substantial grain growth. Consequently, this results in larger grains within the weld metal, accompanied by a reduced grain boundary area from which Widmanstätten austenite can propagate. Moreover,

the increased surface area of the melt, coupled with thermal convection, induces stirring, potentially causing additional nitrogen loss to the surrounding atmosphere. Nevertheless, this loss is counteracted by the deliberate addition of nitrogen to the shielding gas, which favors nucleation of intergranular austenite.

5 Conclusions

Gleeble[®] simulation was conducted on a 6-mm-thick lean duplex stainless steel of UNS S32101 type to investigate the HT-HAZ using varying holding times and cooling rates. Both stationary and travelling arc welding with the GTAW process were performed bead-on-plate on material of the same heat, with and without nitrogen additions to the shielding gas. The ferrite content, weld shape, and grain size or HAZ width were measured on polished and etched cross-sections. The objective was to assess the suitability of these methods for studying the HT-HAZ. In summary, the following conclusions can be drawn:

1. Stationary arc welding resulted in a deviation from the regular semi-circular profiles observed in travelling arc welding. Computational modeling confirmed that the irregular HT-HAZ shape was correlated with the final weld profile.
2. Stationary arc welding rapidly depleted the HAZ of nitrogen, and even with the shortest duration of 0.5 s, the ferrite content became higher than what could be observed with any of the actual travelling arc welds. While this method may be relevant for other studies, it is not suitable for determining the morphology of the HT-HAZ.
3. The weld metal was strongly affected by nitrogen additions to the shielding gas and slightly by the heat input, but the HT-HAZ of the travelling arc welds remained fairly unaffected for the arc energies 0.4–1.2 kJ/mm explored in this work.
4. Solidification cracks were observed at the weld surface of stationary arc welds with nitrogen additions to the shielding gas, potentially resulting from the formation of ‘false nitrogenous pearlite’ due to nitrogen oversaturation.
5. Thermo-mechanical Gleeble[®] simulation of the HT-HAZ closely approximated the results of travelling arc welds performed bead-on-plate. Although the samples did not reach the highest temperatures near the fusion line (liquidus), the average ferrite content of 75–82 vol.-% obtained with water quenching matched the 72–87 vol.-% measured for the HAZ in the travelling arc welds.
6. With a holding time of 0–10 s and water quenching, the grain growth in the Gleeble[®]-simulated HT-HAZ resembled that observed in travelling arc welds with an arc energy of 0.4–1.2 kJ/mm and after stationary arc welding with Ar for a duration of 2.5–10 s.
7. The results in this work are expected to be applicable to other duplex stainless steels.

Acknowledgements Dr. H.C. Ing. Kaj Grönlund at Corr-Control in Avesta, Sweden, performed the EPMA measurements. Dr. Vahid A. Hosseini at Esab AB in Göteborg, Sweden, provided the base for the COMSOL model for the thermal simulation of arc heat treatment. The late Dr. Damian J. Kotecki contributed valuable comments. His expertise and pleasant personality will forever be missed.

Author contribution Dr. E.M. Westin wrote the paper, performed the welding and Gleeble[®] simulations, and the subsequent sample evaluation. Prof. L.G. Westerberg performed the COMSOL simulations. Both authors have read the manuscript and approved of the final version.

Funding Open access funding provided by Lulea University of Technology.

Data Availability The data that support the findings of this study are available on request.

Declarations

Conflicts of interest The authors declare no competing interests.

Open Access This article is licensed under a Creative Commons Attribution 4.0 International License, which permits use, sharing, adaptation, distribution and reproduction in any medium or format, as long as you give appropriate credit to the original author(s) and the source, provide a link to the Creative Commons licence, and indicate if changes were made. The images or other third party material in this article are included in the article’s Creative Commons licence, unless indicated otherwise in a credit line to the material. If material is not included in the article’s Creative Commons licence and your intended use is not permitted by statutory regulation or exceeds the permitted use, you will need to obtain permission directly from the copyright holder. To view a copy of this licence, visit <http://creativecommons.org/licenses/by/4.0/>.

References

1. Kudo T, Tsuge H, Moroishi T (1989) Stress corrosion cracking resistance of 22% Cr duplex stainless steel in simulated sour environments. *Corros* 45(10):831–838. <https://doi.org/10.5006/1.3584990>
2. EN ISO 15156-3 (2020) Petroleum and natural gas industries – materials for use in H₂S-containing environments in oil and gas protection. Part 3: Cracking-resistant CRAs (corrosion resistant alloys) and other alloys. European Committee for Standardization, Brussels, Belgium, p 80
3. Gunn RN (1997) Duplex stainless steels: microstructure, properties and applications. Woodhead Publishing Ltd, Cambridge ISBN 9781855733183
4. Karlsson L (2000) Welding of stainless steels. Duplex and superduplex steels *Weld Int* 14(12):5–11. <https://doi.org/10.1080/09507110009549131>
5. Berglund G, Wilhelmsson P (1989) Fabrication and practical experience of duplex stainless steels. *Mater Des* 10(1):23–28. [https://doi.org/10.1016/0261-3069\(89\)90031-9](https://doi.org/10.1016/0261-3069(89)90031-9)
6. Knyazeva M, Pohl M (2013) Duplex steels: Part I: Genesis, formation, structure. *Metallogr Microstruct Anal* 2(4):113–121. <https://doi.org/10.1007/s13632-013-0066-8>

7. Kotecki DJ (1986) Ferrite control in duplex stainless steel weld metal. *Weld J Res Suppl* 65(10):273s–278s
8. Ferreira PJ, Hertzman S (1991) δ -Ferrite grain growth in simulated high temperature HAZ of three duplex stainless steels. *Proc. Duplex Stainless Steels '91*, Beaune, France. Les Editions de Physique 2:959–966
9. Corolleur A, Fanica A, Passot G (2015) Ferrite content in the heat affected zone of duplex stainless steels. *BHM* 160(9):413–418. <https://doi.org/10.1007/s00501-015-0408-8>
10. Yang Y, Wang Z, Tan H, Hong J, Jiang Y, Jiang L, Li J (2012) Effect of a brief post-weld heat treatment on the microstructure evolution and pitting corrosion of laser beam welded UNS S31803 duplex stainless steel. *Corros Sci* 65(8):472–470. <https://doi.org/10.1016/j.corsci.2012.08.054>
11. Nilsson J-O (1992) Super duplex stainless steels. *Mater Sci Technol* 8(8):685–700. <https://doi.org/10.1179/mst.1992.8.8.685>
12. Nilsson J-O, Wilson B, Josefsson B, Thorvaldsson T (1992) Relationship between pitting corrosion, toughness and microstructure for isothermally heat treated super duplex stainless steel. *Applications of Stainless Steel '92*, vol 1. Stockholm, Sweden, pp 280–289
13. Lee KM, Cho HS, Choi DC (1999) Effect of isothermal treatment of SAF 2205 duplex stainless steel on migration of δ/γ interface boundary and growth of austenite. *J Alloys Comp* 285(1–2):156–161. [https://doi.org/10.1016/S0925-8388\(99\)00014-6](https://doi.org/10.1016/S0925-8388(99)00014-6)
14. El Koussy MR, El Mahallawi IS, Khalifa W, Al Dawood MM, Bueckins M (2004) Effects of thermal aging on microstructure and mechanical properties of duplex stainless steel. *Mater Sci Technol* 20(3):375–381. <https://doi.org/10.1179/174328413X13789824293821>
15. Muthupandi V, Bala Srinivasan P, Shankar V, Seshadri SK, Sundaresan S (2005) Effect of nickel and nitrogen addition on the microstructure and mechanical properties of power beam processed duplex stainless steel (UNS 31803) weld metals. *Mater Lett* 59(18):2305–2309. <https://doi.org/10.1016/j.matlet.2005.03.010>
16. Hertzman S, Ferreira PJ, Brolund B (1997) An experimental and theoretical study of heat-affected zone austenite reformation in three duplex stainless steels. *Metall Mater Trans A* 28(2):277–285. <https://doi.org/10.1007/s11661-997-0130-6>
17. Hertzman S, Symniotis E (1991) Influence of nitrogen content and welding procedure on microstructure and pitting resistance of 22Cr duplex stainless steel. *Proc. Stainless Steels*, Chiba, Japan, ISI, 1085–1092
18. Liljas M (1995) The welding metallurgy of duplex stainless steels. *Proc Duplex Stainless Steels '94*. TWI 2(Paper KV), Glasgow, Scotland, p 15
19. Ogawa T, Koseki T (1989) Effect of composition profiles on metallurgy and corrosion behavior of duplex stainless steel weld metals. *Weld J Res Suppl* 68(5):181s–191s. http://files.aws.org/wj/supplement/WJgamma1989_05_s181.pdf
20. Kotecki DJ (2013) Landmark events in the welding of stainless steels. *Adv Mater Res* 794(9):257–273. <https://doi.org/10.4028/www.scientific.net/AMR.794.257>
21. Hertzman S (2001) The influence of nitrogen on microstructure and properties of highly alloyed stainless steel welds. *ISIJ Int* 41(6):580–589. <https://doi.org/10.2355/isijinternational.41.580>
22. Komizo Y, Ogawa K, Azuma S (1991) HAZ embrittlement in high Cr-Mo duplex stainless steel and the effects of Ni and N. *Weld Int* 5(4):277–282. <https://doi.org/10.1080/09507119109446735>
23. Hsieh R-I, Liou H-Y, Pan Y-T (1999) Weldability of 22% Cr duplex stainless steels. *China Steel Technical Report* 13:14–26
24. Hsieh R-I, Liou H-Y, Pan Y-T (2001) Effects of cooling time and alloying elements on the microstructure of the Gleeble-simulated heat-affected zone of 22% Cr duplex stainless steels. *J Mater Eng Perform* 10(10):526–536. <https://doi.org/10.1361/105994901770344665>
25. Leone GL, Kerr HW (1982) The ferrite to austenite formation in stainless steels. *Weld J Res Suppl* 61(1):13s–21s
26. Dohnke R, Gillessen C, Ladwein T, Reichel U (1991) Ferritic-austenitic duplex stainless steels with improved material's and working properties. *Proc Duplex Stainless Steels '91*, vol 2. Les editions de physique, Beaune, France, pp 1375–1384
27. Kokawa H, Umeda S, Kuwana T (1994) Effects of nitrogen on tensile properties of duplex stainless steel weld metal. *Weld Int* 8(6):531–537. <https://doi.org/10.1080/09507119409548630>
28. Varbai B, Pickle T, Májlinger K (2019) Effect of heat input and role of nitrogen on the phase evolution of 2205 duplex stainless steel weldment. *Int J Pressure Vessels Piping* 176(9):103952. <https://doi.org/10.1016/j.ijpvp.2019.103952>
29. Hosseini VA, Wessman S, Hurtig K, Karlsson L (2016) Nitrogen loss and effects on microstructure in multipass TIG welding of a super duplex stainless steel. *Mater Des* 98(5):88–97. <https://doi.org/10.1016/j.matdes.2016.03.011>
30. Westin EM, Johansson MM, Pettersson RFA (2013) Effect of nitrogen-containing shielding and backing gas on the pitting corrosion resistance of welded lean duplex stainless steel LDX 2101® (EN 1.4162, UNS S32101). *Weld World* 57(7):467–476. <https://doi.org/10.1007/s40194-013-0046-2>
31. Migiakis K, Papadimitriou GD (2009) Effect of nitrogen and nickel on the microstructure and mechanical properties of plasma welded UNS S32760 super-duplex stainless steels. *J Mater Sci* 44(12):6372–6383. <https://doi.org/10.1007/s10853-009-3878-9>
32. Westin EM, Johansson MM, Bylund L-Å, Pettersson RFA (2014) Effect on microstructure and properties of super duplex stainless steel welds when using backing gas containing nitrogen and hydrogen. *Weld World* 58(5/6):347–354. <https://doi.org/10.1007/s40194-014-0120-4>
33. Westin EM, Serrander D (2012) Experience in welding stainless steels for water heater applications. *Weld World* 56(5/6):14–28. <https://doi.org/10.1007/BF03321346>
34. Valiente Bermejo MA, Thalavai Pandian K, Axelsson B, Harati E, Kisielwicz A, Karlsson L (2021) Microstructure of laser metal deposited duplex stainless steel: Influence of shielding gas and heat treatment. *Weld World* 65(3):525–541. <https://doi.org/10.1007/s40194-020-01036-5>
35. Allum C (1992) Nitrogen absorption from welding arcs. *WRC Bulletin* 369:68–83
36. Keskitalo M, Mäntyjärvi K, Sundqvist J, Powell J, Kaplan AFH (2015) Laser welding of duplex stainless steel with nitrogen as shielding gas. *Mater Process Technol* 216(2):381–384. <https://doi.org/10.1016/j.jmatprotec.2014.10.004>
37. Lai R, Cai Y, Wu Y, Li F, Hua X (2016) Influence of absorbed nitrogen on microstructure and corrosion resistance of 2205 duplex stainless steel joint processed by fiber laser welding. *J Mater Process Technol* 231:397–405. <https://doi.org/10.1016/j.jmatprotec.2016.01.016>
38. Baghdadchi A, Hosseini VA, Hurtig K, Karlsson L (2021) Promoting austenite formation in laser welding of duplex stainless steel – Impact of shielding gas and laser reheating. *Weld World* 65:499–511. <https://doi.org/10.1007/s40194-020-01026-7>
39. Wang K, Jiao X, Zhu J, Shao C, Li C (2022) Effect of nitrogen protection on weld metal microstructure and intergranular behavior of S32101 duplex stainless steel 15m water depth hyperbaric laser underwater welding. *Adv Mech Eng* 14(1):1–12. <https://doi.org/10.1177/16878140211072943>

40. Baghdadchi A, Hosseini VA, Valiente Bermejo MA, Axelson B, Harati E, Högstrom M, Karlsson L (2022) Wire laser metal deposition of 22% Cr duplex stainless steel: as-deposited and heat-treated microstructure and mechanical properties. *J Mater Sci* 57(6):9556–9575. <https://doi.org/10.1007/s10853-022-06878-6>
41. Atamert S, King JE (1992) Super duplex stainless steels. Part 1. Heat affected zone microstructures. *Mater Sci Techn* 8(7):896–911. <https://doi.org/10.1179/mst.1992.8.10.896>
42. Yasuda K, Tamaki K, Nakano S, Kobayashi K, Nishiyama N (1986) Metallurgical characteristics of weld metals and corrosion performance of girth weld joints of duplex stainless steel pipes. *Proc. Duplex Stainless Steels '86*, The Hague, The Netherlands. NIL Paper 24:201–212
43. Chen L, Tan H, Wang Z, Li J, Jiang Y (2015) Influence of cooling rate on microstructure evolution and pitting corrosion resistance in the simulated heat-affected zone of 2304 duplex stainless steels. *Corros Sci* 58(5):168–174. <https://doi.org/10.1016/j.corsci.2012.01.018>
44. Yang Y, Guo Y, Liu Y, Li Y, Li J, Jiang Y (2019) The microstructure and pitting resistance of 2002 lean duplex stainless steel after the simulated welding thermal cycle process. *Materials* 12(1):70. <https://doi.org/10.3390/ma12010070>
45. Morales EV, Pozo JA, Olaya L, Kassab E, Ponciano JAC, Ghavami K, Bott LS (2019) Remarks on the evolution and performance of the different austenite morphologies at the simulated HAZs of a 2205 duplex stainless steel. *J Mater Res Technol* 8(5):3936–3949. <https://doi.org/10.1016/j.jmrt.2019.07.002>
46. Hosseini VA, Karlsson L (2019) Physical and kinetic simulation of nitrogen loss in high temperature heat affected zone of duplex stainless steels. *Materialia* 6(6):762–775. <https://doi.org/10.1016/j.mtla.2019.100325>
47. Varbai B, Adonyi Y, Baumer R, Pickle T, Dobránszky J, Májlínger K (2019) Weldability of duplex stainless steels – thermal cycle and nitrogen effects. *Weld J Res Suppl* 98(3):78s–87s. <https://doi.org/10.29391/2019.98.006>
48. Westin EM, Grönlund K, Runnsjö G, Cross CE (2017) Use of electron microprobe analysis to explain metallurgical phenomena and their effect on properties when welding stainless steel. *Weld World* 62(1/2):55–69. <https://doi.org/10.1007/s40194-017-0522-1>
49. Westin EM, Hertzman S (2014) Element distribution in lean duplex stainless steel welds. *Weld World* 58(2):143–160. <https://doi.org/10.1007/s40194-013-0108-5>
50. Sridhar N, Kolts J (1987) Effects of nitrogen on the selective dissolution of a duplex stainless steel. *Corros* 43(11):646–651. <https://doi.org/10.5006/1.3583843>
51. Hosseini VA, Hurtig K, Karlsson L (2020) Bead by bead study of a multipass shielded metal arc-welded super-duplex stainless steel. *Weld World* 64(2):283–299. <https://doi.org/10.1007/s40194-019-00829-7>
52. Hertzman S, Roberts W, Lindenmo M (1986) Microstructure and properties of nitrogen alloyed stainless steel after welding treatments. *Proc. Duplex Stainless Steels '86*. The Hauge, The Netherlands, NIL, Paper 30:257–263
53. Omura T, Kushida T, Kudo T, Hayashi T, Matsuhiro Y, Hikida T (1997) Effect of nitrogen distribution on pitting corrosion resistance in high power laser welded duplex stainless steels. *Tetsu-to-Hagane* 83(9):575–580. https://doi.org/10.2355/tetsutohagane1955.83.9_575
54. Zhang Z, Jing H, Xu L, Han Y, Zhao L (2017) Influence of microstructure and elemental partitioning on pitting corrosion resistance of duplex stainless steel welding joints. *Corros Sci* 394(2):194–210. <https://doi.org/10.1016/j.apsusc.2016.10.047>
55. Liao J (2001) Nitride precipitation in weld HAZs of a duplex stainless steel. *ISIJ Int* 41(5):460–467. <https://doi.org/10.2355/isijinternational.41.460>
56. Chen TH, Yang JR (2002) Microstructural characterization of simulated heat affected zone in a nitrogen-containing 2205 duplex stainless steel. *Mater Sci Eng A* 338(1–2):166–181. [https://doi.org/10.1016/S0921-5093\(02\)00065-5](https://doi.org/10.1016/S0921-5093(02)00065-5)
57. Ramirez AJ, Brandi SD, Lippold JC (2004) Secondary austenite and chromium nitride precipitation in simulated heat affected zones of duplex stainless steels. *Sci Tech Weld Joi* 9(4):301–313. <https://doi.org/10.1179/136217104225021715>
58. Kokawa H, Tsory E, North TH (1995) Nitride precipitation in duplex stainless steel weld metal. *ISIJ Int* 35(10):1277–1283. <https://doi.org/10.2355/isijinternational.35.1277>
59. Hu Y, Shi Y-H, Shen X-Q, Wang Z-M (2017) Microstructure, pitting corrosion resistance and impact toughness of duplex stainless steel underwater dry hyperbaric flux-cored arc welds. *Materials* 10(1443):18. <https://doi.org/10.3390/ma10121443>
60. Jing H, Xu L, Han Y, Zhao L, Zhou C (2017) Effects of nitrogen in shielding gas on microstructure evolution and localized corrosion behavior of duplex stainless steel welding joint. *Appl Surf Sci* 404(5):110–128. <https://doi.org/10.1016/J.APSUSC.2017.01.252>
61. Hoffmeister H, Lothongkum G (1994) Quantitative effects of nitrogen contents and cooling cycles on δ - γ transformation, chromium nitride precipitation and pitting corrosion after weld simulation of duplex stainless steels. *Proc Duplex Stainless Steels '94*, vol 2. Glasgow, Scotland, p 12
62. Lundqvist B, Norberg P, Olsson K (1986) Influence of different welding conditions on mechanical properties and corrosion resistance of Sandvik SAF 2205 (UNS S31803). *Proc Duplex Stainless Steels '86*, vol 10. The Hague, NL, NIL, pp 16–29 (Paper)
63. Liou H-L, Hsieh R-I, Tsai W-T (2002) Microstructure and pitting corrosion in simulated heat-affected zones of duplex stainless steels. *Mater Chem Phys* 74(1):33–42. [https://doi.org/10.1016/S0254-0584\(01\)00409-6](https://doi.org/10.1016/S0254-0584(01)00409-6)
64. Perren RA, Suter T, Solenthaler C, Gullo G, Uggowitzer PJ, Böhni H, Speidel MO (2001) Corrosion resistance of super duplex stainless steels in chloride ion containing environments: Investigations by means of a new microelectrochemical method II. Influence of precipitates. *Corros Sci* 43(4):727–745. [https://doi.org/10.1016/S0010-938X\(00\)00088-3](https://doi.org/10.1016/S0010-938X(00)00088-3)
65. Han Y, Zhang Y, Jing H, Gao Z, Xu L, Zhang Z, Zhao L (2020) Microstructure and corrosion studies on different zones of super duplex stainless steel UNS S32750 weldment. *Front Mater* 7(11):251. <https://doi.org/10.3389/fmats.2020.00251>
66. Jargelius-Pettersson RFA, Hertzman S, Szakalos P, Ferreira PJ (1994) The influence of microstructure in pitting corrosion in autogenous TIG duplex stainless steel welds. *Proc. Duplex Stainless Steels '94*, Glasgow, Scotland, TWI, 461–472
67. Yang Y, Yan B, Li J, Wang J (2011) The effect of large heat input on the microstructure and corrosion behaviour of simulated heat affected zone in 2205 duplex stainless steel. *Corros Sci* 53(11):3756–3763. <https://doi.org/10.1016/j.corsci.2011.07.022>
68. Holländer Pettersson N, Lindell D, Lindberg F, Borgenstam A (2019) Formation of chromium nitride and intragranular austenite in a super duplex stainless steel. *Metall Mater Trans A* 50(12):5594–5601. <https://doi.org/10.1007/s11661-019-05489-2>
69. Hosseini VA, Karlsson L, Hurtig K, Choquet I, Engelberg D, Roy MJ, Kumara C (2017) A novel arc heat treatment technique for producing graded microstructures through controlled temperature gradients. *Mater Des* 121(5):11–23. <https://doi.org/10.1016/j.matdes.2017.02.042>
70. Meadows C, Fritz JD (2005) Understanding stainless steel heat-affected zones. *Weld J* 84(7):26–30

71. Brandi SD (2003) Some aspects of weldability and jointability of duplex stainless steels. *Mater Sci Forum* 426–432(8):4063–4068. <https://doi.org/10.4028/www.scientific.net/MSF.426-432.4063>
72. Pettersson N, Wessman S, Hertzman S, Studer A (2017) High-temperature phase equilibria of duplex stainless steels assessed with a novel in-situ neutron scattering approach. *Metall Mater Trans A* 48(4):1562–1571. <https://doi.org/10.1007/s11661-016-3953-1>
73. Lippold JC, Varol I, Baeslack WA III (1991) Heat affected zone microstructure and properties in commercial duplex stainless steel weldments, *Proc. Duplex Stainless Steels '91*. Les Editions de Physique, Beaune, France 1:383–392
74. Bonnefois B, Charles J, Duoiron F, Soullignac P (1991) How to predict welding properties of duplex stainless steels? *Proc Duplex Stainless Steels '91*, vol 1. Les editions de physique, Beaune, France, pp 347–361
75. Wang H-S (2005) Effect of welding variables on cooling rate and pitting corrosion resistance in super duplex stainless weldments. *Mater Trans* 46(3):593–601. <https://doi.org/10.2320/matertrans.46.593>
76. Nishimoto K, Saida K, Katsuyama O (2006) Prediction of sigma phase precipitation in super duplex stainless steel weldments. *Weld World* 50(3/4):13–28. <https://doi.org/10.1007/BF03263429>
77. Hosseini VA, Bermejo MAV, Gårdstam J, Hurtig K, Karlsson L (2016) Influence of multiple thermal cycles on microstructure of heat-affected zone in TIG-welded super duplex stainless steel. *Weld World* 60(2):233–245. <https://doi.org/10.1007/s40194-016-0300-5>
78. Tao RL, Liu J, Fan GW, Chang X (2015) The study on welding HAZ microstructure of SAF 2507 duplex stainless steel by simulation tests. *Mater Sci Forum* 26(10):277–280. <https://doi.org/10.4028/www.scientific.net/MSF.804.277>
79. Tsuge H, Tarutani Y, Kudo T (1988) The effect of nitrogen on the localized corrosion resistance of duplex stainless steel simulated weldments. *Corrosion* 44(5):305–314. <https://doi.org/10.5006/1.3583942>
80. Lindblom BES, Lundqvist B, Hannerz NE (1991) Grain growth in HAZ of duplex stainless steels. *Scand J Metall* 20(5):305–315
81. Westin EM, Brolund B, Hertzman S (2008) Weldability aspects of a newly developed duplex stainless steel LDX 2101. *Steel Res Int* 79(6):473–481. <https://doi.org/10.1002/srin.200806155>
82. Guo Y, Sun T, Hu J, Jiang Y, Jiang L, Li J (2016) Microstructure evolution and pitting corrosion resistance of the Gleeble-simulated heat-affected zone of a newly developed lean duplex stainless steel. *J Alloys Compd* 658(2):1031–1040. <https://doi.org/10.1016/j.jallcom.2015.10.218>
83. Komenda J, Sandström R (1995) Quantitative characterisation of weld simulated structures in duplex stainless steel SAF 2205. *Acta Stereol* 14(1):29–34. <http://popups.uliege.be/0351-580x/index.php?id=663&file=1&pid=662>. Accessed on 2021–11–09
84. Kim D-C, Ogura T, Yamashita S, Oikawa Y, Saida K (2020) Computer prediction of α/γ phase fraction in multi-pass weld of duplex stainless steel and microstructural improvement welding process. *Mater Des* 196(109154):10. <https://doi.org/10.1016/j.matdes.2020.109154>
85. Yamashita S, Ike K, Yamasaki K, Wang W-G, K, Ogura T, Saida K, (2022) Relationship between ferrite-austenite phase transformation and precipitation behavior of sigma phase in super duplex stainless steel weldment. *Weld World* 66(2):351–362. <https://doi.org/10.1007/s40194-021-01239-4>
86. Cao H-L, Hertzman S (1991) The relationship between impact properties and welding simulated microstructures in three duplex stainless steels. *Proc Duplex Stainless Steels '91*, vol 1. Les editions de physique, Beaune, France, pp 324–363
87. Palmer TA, Elmer JW, Babu SS (2004) Observations of ferrite/austenite transformations in the heat affected zone of 2205 duplex stainless steel spot welds using time resolved X-ray diffraction. *Mater Sci Eng A* 374(1–2):307–321. <https://doi.org/10.1016/j.msea.2004.03.037>
88. Hosseini VA, Karlsson L, Engelberg D, Wessman S (2018) Time temperature-precipitation and property diagrams for super duplex stainless steel weld metals. *Weld World* 62(5):517–533. <https://doi.org/10.1007/s40194-018-0548-z>
89. Hosseini VA, Karlsson L, Örnek C, Reccagni P, Wessman S, Engelberg D (2018) Microstructure and functionality of a uniquely graded super duplex stainless steel designed by a novel arc heat treatment method. *Mater Charact* 139(5):390–400. <https://doi.org/10.1016/j.matchar.2018.03.024>
90. Putz A, Hosseini VA, Westin EM, Enzinger N (2020) Microstructure investigation of duplex stainless steel welds using arc heat treatment technique. *Weld World* 64(7):1135–1147. <https://doi.org/10.1007/s40194-020-00906-2>
91. Cederberg E, Hosseini VA, Kumara C, Karlsson L (2020) Physical simulation of additively manufactured super duplex stainless steels – microstructure and properties. *Additive Manuf* 34(8):101269. <https://doi.org/10.1016/j.addma.2020.101269>
92. Hertzman S, Jargelius Pettersson R, Blom R, Kivineva E, Eriksson J (1996) Influence of shielding gas composition and welding parameters on the N-content and corrosion properties of welds in N-alloyed stainless steel grades. *ISIJ Int* 35(7):968–976. https://www.jstage.jst.go.jp/article/isijinternational1989/36/7/36_7_968/pdf
93. Hertzman S, Wessman S (1999) An experimental and theoretical study of nitrogen flux in stainless steel TIG welds. *Mater Sci Forum* 318–320(10):579–590. <https://doi.org/10.4028/www.scientific.net/MSF.318-320.579>
94. Hertzman S (2001) The influence of nitrogen on microstructure and properties of highly alloyed stainless steel welds. *ISIJ Int* 41(6):580–589. https://www.jstage.jst.go.jp/article/isijinternational1989/41/6/41_6_580/pdf
95. Hertzman S, Bonnefois B, Coudreuse L (2004) ECSC Steel RTD Programme final report: improvement of weld properties of high nitrogen alloyed stainless steels. 7210-PR/177. Publications Office, 201pp.
96. Grönlund K, Runnsjö G (2002) An electron micro/macro probe system for elemental concentration mapping. *CETAS Conference on Progress of Analytical Chemistry*, Luxembourg, p 4
97. Runnsjö G (1981) Carbon and nitrogen in steel. Determination of content and distribution by electron probe microanalysis (EPMA). Abstracts of Uppsala dissertations from the Faculty of Science. Uppsala, Sweden. ISBN 91–554–1145–2
98. Valiente Bermejo MA, Hurtig K, Eyzop D, Karlsson L (2019) A new approach to the study of multi-pass welds – microstructure and properties of welded 20-mm-thick superduplex stainless steel. *Appl Sci* 9(3):1050. <https://doi.org/10.3390/app9061050>
99. Westin EM, Olsson C-OA, Hertzman S (2008) Weld oxide formation on lean duplex stainless steel. *Corros Sci* 50(9):2620–2634. <https://doi.org/10.1016/j.corsci.2008.06.024>
100. Kumara C (2016) Modelling of the temperature field in TIG arc heat treated super duplex stainless steel samples. Master's thesis at University West, Trollhättan, Sweden. Retrieved from <http://urn.kb.se/resolve?urn=urn:nbn:se:hv:diva-9590> on 2023–04–14.
101. Vattappara K, Hosseini VA, Joseph C, Hanning F, Andersson J (2021) Physical and thermodynamic simulations of gamma-prime precipitation in Haynes® 282® using arc heat treatment. *J Alloys Compd* 870:159484, 11. <https://doi.org/10.1016/j.jallcom.2021.1594840925-8388>
102. Westin EM, Wessman S (2023) Characteristics of high-temperature heat-affected zones in duplex stainless steels. Submitted to *Welding in the World*. IIW Doc. IX-2804-2023 presented at the IIW Annual Assembly in Singapore, p 13

103. Fuertes N, Bengtsson R, Pettersson R, Rohwerder, (2016) Use of SVET to evaluate corrosion resistance of heat tints on stainless steel welded joints and effect of different post-weld cleaning treatments. *Mater Corros* 68(1):7–19. <https://doi.org/10.1002/maco.201609048>
104. Kujanpää V, Suutala N, Takalo T, Moisio T (1979) Correlation between solidification cracking and microstructure in austenitic and austenitic-ferritic stainless steel. *Weld Res Int* 9(2):55–76
105. Kujanpää V, Suutala N, Takalo T, Moisio T (1980) Solidification cracking – Estimation of the susceptibility of austenitic and austenitic-ferritic stainless steel welds. *Metal Constr* 12(6):282–285
106. Torkhov GF, Slyshankova VA, Ul'yanin EA, Sherevera AV (1978) Structure and properties of high-nitrogen corrosion-resistant austenitic steels. *Met Sci Heat Treat* 20(11):887–890. <https://doi.org/10.1007/BF00713747>
107. Rashec TV, Dzhambazova LP, Kovacheva RS, Andreev CA (1981) Processes of precipitation and intercrystalline corrosion in high-nitrogen Cr-Mn steels after isothermal annealing. *Met Sci Heat Treat* 23(5):310–313. <https://doi.org/10.1007/BF00700539>
108. Vanderschaeve F, Taillard R, Foct J (1995) Discontinuous precipitation of Cr₂N in a high-nitrogen chromium-manganese austenitic stainless steel. *J Mat Sci* 30(12):6035–6046. <https://doi.org/10.1007/BF01151525>
109. Prohaska M (2012) Unpublished work
110. Gupta A, Kumar A, Baskaran T, Arya SB, Khatirkar RK (2018) Effect of heat input on microstructure and corrosion behavior of duplex stainless steel shielded metal arc welds. *Trans Indian Inst Met* 71(2):1595–1606. <https://doi.org/10.1007/s12666-018-1294-z>
111. Cui S, Pang S, Pang D, Zhang Z (2021) Influence of welding speeds on the morphology, mechanical properties and microstructure of 2205 DSS welded joint by K-TIG welding. *Mater* 14(3426):10. <https://doi.org/10.3390/ma14123426>
112. Rodriguez BR, Miranda A, Gonzalez D, Rolando Praga R, Hurtado E (2020) Maintenance of the austenite/ferrite ratio balance in GTAW DSS joints through process parameters optimization. *Materials* 13(3):780–796. <https://doi.org/10.3390/ma13030780>
113. Soares da Fonseca G, Rodrigues Barbosa LO, Alves Ferreira E, Xavier CR, Adilson de Castro J (2017) Microstructural, mechanical, and electrochemical analysis of duplex and superduplex stainless steels welded with the autogenous TIG process using different heat input. *Metals* 358(7):21. <https://doi.org/10.3390/met7120538>
114. Huang J, Pan W, Chen J, Shao Y, Yang M, Zhang Y (2018) The transient behaviours of free surface in a fully penetrated weld pool in gas tungsten arc welding. *J Manuf Process* 36(11):405–416. <https://doi.org/10.1016/j.jmapro.2018.10.024>
115. ISO/TR 22824 (2023) Welding — Best practices for specification and measurement of ferrite in stainless steel weld metal. European Committee for Standardization, 2nd edn. Brussels, Belgium, p 42
116. Adonyi Y (2006) Heat-affected zone characterization by physical simulations. *Weld J* 85(10):42–47
117. Westin EM (2010) Pitting corrosion resistance of GTA welded lean duplex stainless steel. *Weld World* 54(11/12):R308–R321. <https://doi.org/10.1007/BF03266745>
118. Geng S, Sun J, Guo L, Wang H (2015) Evolution of microstructure and corrosion behavior in 2205 duplex stainless steel GTA-welding joint. *J Manuf Process* 19(8):32–37. <https://doi.org/10.1016/j.jmapro.2015.03.009>
119. Jargelius-Pettersson R, Hertzman S, Szakalos P, Ferreira PJ (1994) The influence of microstructure in pitting corrosion in autogenous TIG duplex stainless steel welds. *Proc. Duplex Stainless Steels '94*, Glasgow, Scotland, TWI, 461–472

Publisher's Note Springer Nature remains neutral with regard to jurisdictional claims in published maps and institutional affiliations.